Conformal IRS-Empowered MIMO-OFDM: Channel Estimation and Environment Mapping

Yuxing Lin, *Student Member, IEEE*, Shi Jin, *Senior Member, IEEE*,
Michail Matthaiou, *Senior Member, IEEE*, and Xiaohu You, *Fellow, IEEE*

Abstract—We consider the channel estimation and environment mapping problems in multiple-input multiple-output orthogonal frequency division multiplexing systems empowered by intelligent reconfigurable surfaces (IRSs). In order to acquire more in-depth environmental information, as well as, to flexibly take into account existing real-life infrastructure, we propose a novel three-dimensional conformal IRS architecture consisting of reflective unit cells distributed on curved surfaces. We model the training signal as a third-order canonical polyadic tensor and construct a tensor factorization problem. Given specific conditions on the allocated temporal-frequency training resources, we develop four channel estimation approaches, i.e., least squares, direct, wideband direct and wideband subspace methods, by leveraging tensor techniques and nonlinear system solvers. By fully exploiting the characteristics of conformal IRSs, we propose two decoupling modes to precisely recover the multipath parameters without ambiguities, which cannot be supported by the traditional IRS planar topologies. We implement scatterer mapping and user positioning tasks based on precise parameter estimates. Simulation results indicate that the proposed conformal IRS structure and estimation schemes can recover the channel state information with remarkable accuracy, thereby offering a centimeter-level resolution of environment mapping.

Index Terms—Channel estimation, cascaded parameter decoupling, conformal IRSs, environment mapping.

I. INTRODUCTION

MILLIMETER wave (30–300 GHz) technologies have been widely investigated as a promising candidate for tackling the seamless data traffic deluge and frequency resource shortage in the fifth generation (5G) era [1]. As one of the potential development directions of the future

sixth generation (6G), exploiting the high-frequency spectrum, e.g., terahertz (0.1–10 THz), has also attracted intensive attention [2]. Multiple-input multiple-output (MIMO) arrays can be integrated into high-frequency wireless systems with a miniaturized implementation, providing remarkable beamforming gains [3]. For the sake of addressing the limited coverage and line-of-sight (LoS) blocking problems, intelligent reconfigurable surfaces (IRSs) have been recently researched to help establishing additional non-line-of-sight (NLoS) links [4].

IRSs can improve the quality and coverage of radio propagation by providing supplementary channels, contributing to the full coverage and broadband connectivity of future wireless networks [5]. An IRS architecture, typically a programmable metasurface, is composed of a massive number of unit cells that can independently interact with the incident signals [6], [7]. The reflection amplitudes and phase shifts of the IRS reflectors can be dynamically reconfigured by a digital controller to artificially customize the electromagnetic responses of the reflected waves [8]. In this way, IRSs can help constructing a smart propagation environment, providing additional degrees of freedom for transceiver design and network optimization [9]. Recently, IRSs have been integrated into numerous applications to improve the system capacity or eliminate inter-cluster interference, e.g., MIMO detection, non-orthogonal multiple access, physical layer security and radio localization and mapping [10]–[13]. Note that these services require exact knowledge of the channel parameters to fully reap the potential of IRSs, thereby entailing fundamental challenges to the channel estimation problem with fully passive IRS modules.

We now delineate the following relevant works: A compressed sensing (CS) strategy with predefined on-grid codebooks was proposed in [14]. An atomic norm denoising scheme with infinite-resolution codebooks was proposed in [15]. A tensor-based strategy that decomposes the cascaded channel by iterative updates was presented in [16]. A binary-reflection controlled least squares (LS) protocol supported by switchable unit cells was presented in [17]. A three-phase training framework with linear minimum mean square error (LMMSE) estimators was developed in [18]. A joint matrix factorization and completion scheme that adopts the approximate message passing (AMP) and Riemannian gradient method was developed in [19]. A matrix-calibration-based factorization that exploits the long-term channel information with the Bayesian inference framework was proposed in [20]. Most of these works estimate the separated channels from

the base station (BS) or user equipment (UE) to the IRS plane, which, however, induces inevitable ambiguities due to the passive nature of reflectors. These estimation uncertainties hinder the exact recovery of multipath parameters, limiting the integration of IRSs into environment-dependent applications [10]–[13]. To tackle this problem, a hybrid IRS layout, composed of both passive and active unit cells, was designed in [21], [22], where a tensor completion algorithm and a deep learning network were proposed respectively. Furthermore, by applying additional pilot sounding procedure or anchor nodes equipped with sensing antennas, some works estimated the channel coefficients in a large timescale [23], [24]. Although these works eliminate the estimation uncertainties, they entail extra hardware complexity and training overhead, thereby raising challenges to practical IRS design and training resource allocation.

In this paper, we consider the channel estimation problem of IRS-empowered MIMO orthogonal frequency division multiplexing (OFDM) systems. We propose a novel three-dimensional (3-D) conformal IRS architecture composed of passive unit cells with distinct coordinates and orientations, which can be regarded as a generalized concept of the twin-IRS structure consisting of two IRS planes proposed in our prior work [25]. This topological design can not only better fit the curved surfaces of communication infrastructure, but also, more significantly, perceive the environmental information of the 3-D real world. Specifically, the conformal IRSs enable the processor to accurately retrieve the cascaded channel coefficients and parameters along three orthogonal spatial directions. By leveraging nonlinear system solvers, we can exactly recover the individual multipath parameters, e.g., angles of arrival (AoAs), angle of departure (AoDs) and time delays. Unlike some existing works that rely on strong assumptions, e.g., the existence of LoS paths with parameters determined by *a priori* device configurations [26], [27], the proposed conformal IRSs are able to decouple the cascaded parameters of realistic channels, thereby supporting a centimeter-level resolution of environment mapping. The main contributions of this paper are summarized as follows:

- We propose a 3-D conformal IRS structure configured on a curved surface, modeling its reflector array response as a combination of phase shift and radiated power factors. The characteristics of conformal IRSs, e.g., shadow effect and coverage region, are analyzed. Moreover, we model the training signal as a third-order canonical polyadic (CP) tensor, and transform the channel estimation problem into a tensor factorization task [28], [29]. By applying a beamspace beamforming strategy at the BS/UE antennas, we obtain the corresponding angular parameters through the 2-D (unitary) ESPRIT algorithm.
- Provided that there are sufficient training frames, we apply a least squares (LS) method to decompose the BS-IRS-UE channel, retrieving the cascaded spatial parameters along three orthogonal directions. By leveraging the characteristics of power radiation pattern and phase shifts among multipath signals, we develop two decoupling schemes, namely "All" and "Pair" modes,

to factorize the cascaded parameters. By applying the nonlinear solver, i.e., Levenberg-Marquardt algorithm (LMA), we efficiently complete the recovery of angular parameters without estimation ambiguities or additional hardware complexity.

- Whenever there are insufficient training frames, we fully exploit in-depth information provided by conformal IRS topologies to develop channel estimation schemes. In the narrowband training scenario, we construct optimization objectives and constraints based on the power radiation pattern. By applying intelligent algorithms, e.g., particle swarm optimization (PSO), we directly recover the channel parameters from the compressed cascaded IRS response vectors. In the wideband training scenario, by leveraging the frequency-sensitive characteristics of practical reflectors [30], we propose two different approaches based on the direct optimization and kernel subspace derivation, respectively.
- By determining the transformation rules of local-global systems, we implement the mapping of actual channel path directions from the estimated angular parameters. By leveraging the quasi-optical propagation features of mmWave frequencies, we exactly decouple the cascaded temporal parameters to realize a precise 3-D localization of the UE and scatterers with a centimeter-level resolution. Moreover, by modeling the rotation procedure of devices, we uniquely recover the orientation of UE antennas with a $0.1°$-level resolution.

Simulation results indicate that the proposed channel estimation schemes can achieve considerable performance of parameter recovery even with limited training measurements. More importantly, the proposed 3-D conformal IRS structure can decouple the cascaded parameters without estimation uncertainties, supporting a high-resolution environment mapping.

The rest of the paper is organized as follows: Section II introduces the IRS-empowered MIMO-OFDM system and the proposed 3-D conformal IRS model. Section III presents the channel estimation schemes with sufficient temporal measurements. Section IV presents the channel estimation schemes with limited training frames. Section V discusses the application of environment mapping based on the estimated channel information. Section VI presents the numerical results of channel estimation and parameter recovery schemes, as well as, the performance of environment mapping. Section VII draws the most important conclusions.

Notations: $\mathbf{a}$, $\mathbf{A}$, $\mathcal{A}$ and $\mathbb{A}$ denote vectors, matrices, tensors and element sets, respectively; $(\cdot)^T$, $(\cdot)^*$, $(\cdot)^H$ and $(\cdot)^\dagger$ denote the transpose, conjugate, Hermitian transpose and pseudo-inverse, respectively; $\otimes$, $\odot$, $\circledast$ and $\circ$ denote the Kronecker, Khatri-Rao, Hadamard and tensor outer products, respectively; $\mathrm{abs}(\cdot)$, $\arg(\cdot)$, $|\cdot|$ and $\angle(\cdot)$ denote the *element-wise* absolute value, measured phase, modulus and true phase, respectively; $\bullet$ and $\times$ denote the vectorial dot and cross products, respectively; $\|\cdot\|_2$, $\|\cdot\|_\mathrm{F}$ denote the 2-norm and Frobenius-norm, respectively; $\mathrm{Diag}(\cdot)$ denotes a diagonal matrix formed by the argument vector; $\ker(\cdot)$ and $\dim(\cdot)$ denote the kernel and dimensionality, respectively; $\mathbf{0}_{m\times n}$, $\mathbf{I}_n$ and $\mathbf{e}_{N,n}$ denote all-zeros matrices, identity matrices and basis unit vectors,
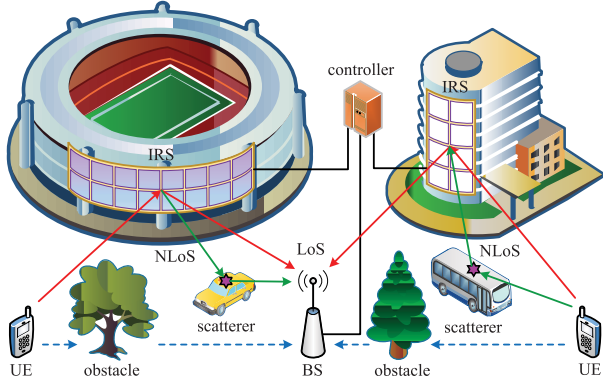
Fig. 1. An IRS-empowered MIMO-OFDM system, where the BS communicates with the UE via the IRS, while the direct UE-to-BS link is assumed to be blocked. The IRS reflection coefficients are configured by the BS through the controller.
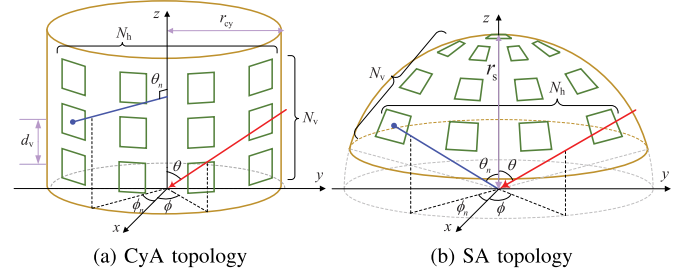

(a) CyA topology (b) SA topology

Fig. 2. Two example designs of the conformal IRS architecture. Red arrow: signal wave with azimuth/elevation angles $\{\phi, \theta\}$; Blue arrow: orientation vector of the nth element with azimuth/elevation angles $\{\phi_n, \theta_n\}$. (a) CyA: $N_{\rm v}$ concentric bows with a radius $r_{\rm cy}$ and an interspacing $d_{\rm v}$; each contains $N_{\rm h}$ elements. (b) SA: Equiangular distribution along $N_{\rm v}$ parallels and $N_{\rm h}$ meridians with a radius $r_{\rm s}$.

respectively; $C_n^2 \triangleq n(n-1)/2$, $\mathcal{I}(n) \triangleq \{1, \ldots, n\}$; $\mathcal{U}(a, b)$ and $\mathcal{CN}(\mu, \sigma^2)$ denote the uniform and complex normal distributions, respectively; $\mathrm{Matr}(\boldsymbol{\mathcal{A}}; [k_1, \ldots, k_P], [k_{P+1}, \ldots, k_N])$ denotes a matricization that unfolds $\boldsymbol{\mathcal{A}} \in \mathbb{C}^{I_1 \times \cdots \times I_N}$ into $\mathbf{A} \in \mathbb{C}^{\prod_{p=1}^{P} I_{k_p} \times \prod_{q=P+1}^{N} I_{k_q}}$; $\boldsymbol{\mathcal{A}} \times_n \mathbf{U}$ denotes the mode-n tensor-matrix product [31].

II. SYSTEM MODEL

We consider an IRS-empowered MIMO-OFDM system as illustrated in Fig. 1, where one BS equipped with $N_{\rm B}$ antennas and $M_{\rm B}$ radio frequency chains (RFCs) communicates with one UE equipped with $N_{\rm U}$ antennas and $M_{\rm U}$ RFCs. The system occupies K subcarriers with a central carrier frequency $f_{\rm c}$ and a bandwidth $f_{\rm s}$. The direct UE-to-BS link is assumed to be obstructed as in the vast body of related literature [14]–[16]. In practice, the BS-UE channel can be efficiently removed by considering two signals with different IRS coefficients and mutually subtracting them. The proposed channel estimation schemes are still applicable.

Unlike most studies that consider one-dimensional (1-D) or two-dimensional (2-D) IRS structures [14]–[27], we propose a 3-D *conformal IRS* architecture with $N_{\rm I}$ reflectors distributed on a curved surface. Two examples of conformal topologies, i.e., cylindrical array (CyA) and spherical array (SA), are shown in Fig. 2(a), (b), respectively. The conformal IRSs can better fit the shape of the communication devices and environmental infrastructure (buildings, vehicles, etc.), supporting a more flexible deployment of IRSs. More significantly, this design is able to comprehensively perceive the real-world environment information thanks to its 3-D structure, thereby facilitating in-depth environment mapping that cannot be supported by traditional IRSs.

We focus on an uplink training transmission for channel estimation with in total $P_{\rm tr}$ training frames, where each frame includes $Q_{\rm tr}$ time slots. During the qth time slot of each frame, the UE transmits pilot symbols $\mathbf{x}_{k,q} \in \mathbb{C}^{M_{\rm U}}$ precoded by $\mathbf{F}_{k,q} \in \mathbb{C}^{N_{\rm U} \times M_{\rm U}}$. The BS combines the received signal by $\mathbf{W}_k \in \mathbb{C}^{N_{\rm B} \times M_{\rm tr}}$ with $M_{\rm tr} \leq M_{\rm B}$ parallel streams. The IRS unit cells utilize dynamic reflection coefficients $\{\psi_{k,n}\}_{n=1}^{N_{\rm I}} \in \mathbb{C}^{P_{\rm tr}}$ across the training frames, while $K_{\rm tr}$ out of K subcarriers

are allocated for training. Then, the received training signal within the qth time slot of the pth frame at the kth subcarrier can be represented as

$$\mathbf{y}_{k,p,q} = \mathbf{W}_k^H \mathbf{H}_{\mathrm{BI},k} \mathrm{Diag}([\boldsymbol{\Psi}_k]_{p,:}) \mathbf{H}_{\mathrm{IU},k} \mathbf{F}_{k,q} \mathbf{x}_{k,q} + \mathbf{n}_{k,p,q},$$
(1)

where $\boldsymbol{\Psi}_k \triangleq [\boldsymbol{\psi}_{k,1}, \ldots, \boldsymbol{\psi}_{k,N_{\rm I}}] \in \mathbb{C}^{P_{\rm tr} \times N_{\rm I}}$ denotes the IRS training pattern; $\mathbf{n}_{k,p,q} \in \mathbb{C}^{M_{\rm tr}}$ is the additive noise; $\mathbf{H}_{\mathrm{BI},k} \in \mathbb{C}^{N_{\rm B} \times N_{\rm I}}$ and $\mathbf{H}_{\mathrm{IU},k} \in \mathbb{C}^{N_{\rm I} \times N_{\rm U}}$ denote the one-hop IRS-to-BS and UE-to-IRS channels at the kth subcarrier, respectively.

Assuming that the system works at the mmWave frequencies, the spatially sparse channels $\mathbf{H}_{\mathrm{BI},k}$ and $\mathbf{H}_{\mathrm{IU},k}$ can be defined by the Saleh-Valenzuela model as [14], [15], [21]–[23]

$$\mathbf{H}_{\mathrm{BI},k} = \sum_{\ell_{\rm t}=1}^{L_{\mathrm{BI}}} \beta_{\mathrm{BI},k,\ell_{\rm t}} \mathbf{a}_{\rm B}(\phi_{\mathrm{B},\ell_{\rm t}}, \theta_{\mathrm{B},\ell_{\rm t}}) \mathbf{a}_{\rm I}^H(\phi_{\mathrm{t},\ell_{\rm t}}, \theta_{\mathrm{t},\ell_{\rm t}})$$
$$= \mathbf{A}_{\rm B} \mathrm{Diag}(\boldsymbol{\beta}_{\mathrm{BI},k}) \mathbf{A}_{\rm t}^H, \tag{2a}$$

$$\mathbf{H}_{\mathrm{IU},k} = \sum_{\ell_{\rm r}=1}^{L_{\mathrm{IU}}} \beta_{\mathrm{IU},k,\ell_{\rm r}} \mathbf{a}_{\rm I}(\phi_{\mathrm{r},\ell_{\rm r}}, \theta_{\mathrm{r},\ell_{\rm r}}) \mathbf{a}_{\rm U}^H(\phi_{\mathrm{U},\ell_{\rm r}}, \theta_{\mathrm{U},\ell_{\rm r}}),$$
$$= \mathbf{A}_{\rm r} \mathrm{Diag}(\boldsymbol{\beta}_{\mathrm{IU},k}) \mathbf{A}_{\rm U}^H, \tag{2b}$$

where $L_{\mathrm{BI(IU)}}$ denotes the number of paths; $\{\beta_{\mathrm{BI},k,\ell_{\rm t}} \triangleq \alpha_{\mathrm{BI},\ell_{\rm t}} e^{-j \frac{2\pi k f_{\rm s}}{K} \tau_{\mathrm{BI},\ell_{\rm t}}}, \beta_{\mathrm{IU},k,\ell_{\rm r}} \triangleq \alpha_{\mathrm{IU},\ell_{\rm r}} e^{-j \frac{2\pi k f_{\rm s}}{K} \tau_{\mathrm{IU},\ell_{\rm r}}}\}$ denote the equivalent path gains with $\{\alpha_{\mathrm{BI},\ell_{\rm r}}, \alpha_{\mathrm{IU},\ell_{\rm r}}\}$ and $\{\tau_{\mathrm{BI},\ell_{\rm t}}, \tau_{\mathrm{IU},\ell_{\rm r}}\}$ being the complex gains and time delays, respectively; $\{\phi(\theta)_{\mathrm{B},\ell_{\rm t}}, \phi(\theta)_{\mathrm{U},\ell_{\rm r}}\}$ denote the azimuth (elevation) AoAs and AoDs at the BS and UE, respectively; $\{\phi(\theta)_{\mathrm{r},\ell_{\rm r}}, \phi(\theta)_{\mathrm{t},\ell_{\rm t}}\}$ denote the azimuth (elevation) AoAs and AoDs at the IRS side, respectively; $\mathbf{a}_{\mathrm{B(U)}}(\phi, \theta) \in \mathbb{C}^{N_{\mathrm{B(U)}}}$ and $\mathbf{a}_{\rm I}(\phi, \theta) \in \mathbb{C}^{N_{\rm I}}$ denote the array response vectors of BS (UE) antennas and conformal IRS, respectively; $\mathbf{A}_{\mathrm{B(U)}} \in \mathbb{C}^{N_{\mathrm{B(U)}} \times L_{\mathrm{BI(IU)}}}$ and $\mathbf{A}_{\mathrm{t(r)}} \in \mathbb{C}^{N_{\rm I} \times L_{\mathrm{BI(IU)}}}$ concatenate the steering vectors corresponding to all the channel paths; $\boldsymbol{\beta}_{\mathrm{BI(IU)},k} \in \mathbb{C}^{L_{\mathrm{BI(IU)}}}$ concatenates the equivalent path gains. Note that $\mathbf{H}_{\mathrm{BI(IU)},k}$ may contain one kind of the LoS and NLoS components or both of them.

Due to the exacerbated loss of mmWave propagation, only the NLoS paths scattered once are considered.[1]

The passive reflectors of a conformal IRS can be arbitrarily arranged on the curved surface. The nth element is located at the coordinates $\boldsymbol{\mu}_n \in \mathbb{R}^3$, while its orientation, defined as the normal direction of the unit cell, is denoted by $\boldsymbol{\nu}_n \in \mathbb{R}^3$. Specifically, the elemental locations and orientations of the CyA and SA topologies in Fig. 2(a), (b) are respectively defined as

$$\text{CyA:} \begin{cases} \boldsymbol{\mu}_n = [r_{\text{cy}}\cos\phi_{n_{\text{h}}}, r_{\text{cy}}\sin\phi_{n_{\text{h}}}, h_{n_{\text{v}}}]^T, \\ \boldsymbol{\nu}_n = [\cos\phi_{n_{\text{h}}}, \sin\phi_{n_{\text{h}}}, 0]^T, \end{cases} \tag{3a}$$

$$\text{SA:} \begin{cases} \boldsymbol{\mu}_n = r_{\text{s}}[\cos\phi_{n_{\text{h}}}\sin\theta_{n_{\text{v}}}, \sin\phi_{n_{\text{h}}}\sin\theta_{n_{\text{v}}}, \cos\theta_{n_{\text{v}}}]^T, \\ \boldsymbol{\nu}_n = [\cos\phi_{n_{\text{h}}}\sin\theta_{n_{\text{v}}}, \sin\phi_{n_{\text{h}}}\sin\theta_{n_{\text{v}}}, \cos\theta_{n_{\text{v}}}]^T, \end{cases} \tag{3b}$$

where r_{cy}, r_{s} denote the radii of the cylinder and sphere, respectively; $\{\phi_{n_{\text{h}}}, h_{n_{\text{v}}}\}$ denote the azimuth angle and elevation height of the $(n_{\text{h}}, n_{\text{v}})$th entry of the CyA, respectively; $\{\phi_{n_{\text{h}}}, \theta_{n_{\text{v}}}\}$ denote the azimuth and elevation angles of the $(n_{\text{h}}, n_{\text{v}})$th entry of the SA, respectively; the 2-D tuple $(n_{\text{h}}, n_{\text{v}})$ is mapped to the index n as $n \triangleq (n_{\text{h}} - 1)N_{\text{v}} + n_{\text{v}}$ with $N_{\text{I}} = N_{\text{h}}N_{\text{v}}$. For a uniformly-distributed CyA, $\phi_{n_{\text{h}}} = \phi_{\text{lb}} + \frac{\phi_{\text{ub}} - \phi_{\text{lb}}}{N_{\text{h}} - 1}(n_{\text{h}} - 1)$, $h_{n_{\text{v}}} = n_{\text{v}}d_{\text{v}}$ with $\phi_{\text{lb(ub)}}$ and d_{v} being the lower (upper) bound of azimuth angles and elevation inter-element spacing, respectively. For a uniformly-distributed SA with equal-angle partitions, $\phi_{n_{\text{h}}} = \phi_{\text{lb}} + \frac{\phi_{\text{ub}} - \phi_{\text{lb}}}{N_{\text{h}}}n_{\text{h}}$, $\theta_{n_{\text{v}}} = \theta_{\text{lb}} + \frac{\theta_{\text{ub}} - \theta_{\text{lb}}}{N_{\text{v}}}n_{\text{v}}$ with $\phi_{\text{lb(ub)}}$ and $\theta_{\text{lb(ub)}}$ being the lower (upper) bound of azimuth and elevation angles, respectively.[2]

For one response vector of the conformal IRS array, its phase term is determined by the phase-shift difference along the array aperture, whilst its magnitude term is characterized by the *power radiation pattern* of the reflectors. The radiation pattern defines the variation rule of the power radiated or received by the unit cells with respect to the wave direction [35], [36]. For one signal component with a unit direction vector $\mathbf{d}(\phi, \theta) \triangleq [\cos\phi\sin\theta, \sin\phi\sin\theta, \cos\theta]^T$, the corresponding IRS array response can be represented as

$$\mathbf{a}_{\text{I}}(\phi, \theta) \triangleq \mathbf{p}_{\text{I}}(\phi, \theta) \circledast \mathbf{g}_{\text{I}}(\phi, \theta), \tag{4a}$$

$$\mathbf{p}_{\text{I}}(\phi, \theta) \triangleq \left[e^{j\frac{2\pi}{\lambda_c}\boldsymbol{\mu}_1^T\mathbf{d}(\phi,\theta)}, \dots, e^{j\frac{2\pi}{\lambda_c}\boldsymbol{\mu}_{N_{\text{I}}}^T\mathbf{d}(\phi,\theta)} \right]^T, \tag{4b}$$

$$\mathbf{g}_{\text{I}}(\phi, \theta) \triangleq \left[f_+^{\frac{\epsilon}{2}}(\boldsymbol{\nu}_1^T\mathbf{d}(\phi,\theta)), \dots, f_+^{\frac{\epsilon}{2}}(\boldsymbol{\nu}_{N_{\text{I}}}^T\mathbf{d}(\phi,\theta)) \right]^T, \tag{4c}$$

---

[1]Generally, the second-order rays have a power degradation of 10–20 dB relative to the first-order ones, which can be identified and filtered out along with the diffuse scattering components [32]. Moreover, the contribution of the higher-order rays to the total received energy is about 2%–10% and is thus negligible [33], [34].

[2]The far-field condition of (2), (3) generally holds with $d \geq \frac{2D^2}{\lambda}$, where d, D and λ denote the distance between the transmitter and the center of the IRS array, the largest dimension of the IRS array and the signal wavelength, respectively [35]. Moreover, $d = 5\lambda$ can be regarded as the lower bound of the near field of the IRS array. If the IRS is too small to fulfill the condition $\frac{2D^2}{\lambda} > 5\lambda$, then the IRS operates only in the far-field region for distances $> 5\lambda$ [36]. Specifically, the array aperture D^2 can be approximated by $r_{\text{cy}}(\phi_{\text{ub}} - \phi_{\text{lb}})d_{\text{v}}N_{\text{v}}$ and $r_{\text{s}}^2(\phi_{\text{ub}} - \phi_{\text{lb}})(\cos\theta_{\text{lb}} - \cos\theta_{\text{ub}})$ for CyA and SA topologies, respectively.

---

where $\epsilon \geq 0$ is the power radiation coefficient ($\epsilon = 0$ corresponds to ideal omnidirectional reflectors); $f_+(x) \triangleq \max(x, 0)$ is the ramp function. Physically, the definition of $\mathbf{g}_{\text{I}}(\cdot)$ indicates that the radiated power level is inversely proportional to the angle between the signal direction and the unit cell orientation [6], [7]. Note that for a traditional IRS composed of reflectors with identical orientations, its amplitude response $\mathbf{g}_{\text{I}}(\phi, \theta)$ degenerates into a scalar coefficient $g_{\text{I}}(\phi, \theta)$. Unfortunately, this scalar term usually gets mized with the path gains, and is difficult to be directly retrieved. By contrast, the conformal IRS supports the extraction of the power radiation pattern, providing more information to the channel estimation procedure.

Remark 1: Note that $f_+(\boldsymbol{\nu}_n^T\mathbf{d}(\phi, \theta))$ physically corresponds to the fact that the IRS reflectors normally cannot reflect or refract incoming signals from their backside. This is due to the shielding phenomenon of opaque substrates or carriers, referred to as a *shadow effect* [37], [38]. For each pair of paths $(\ell_{\text{t}}, \ell_{\text{r}})$, an effective link via the IRS unit cell can be established only if

$$\min\left(\boldsymbol{\nu}_n^T\mathbf{d}(\phi_{\text{t},\ell_{\text{t}}}, \theta_{\text{t},\ell_{\text{t}}}), \boldsymbol{\nu}_n^T\mathbf{d}(\phi_{\text{r},\ell_{\text{r}}}, \theta_{\text{r},\ell_{\text{r}}})\right) > 0, \quad \exists n \in \mathcal{I}(N_{\text{I}}). \tag{5}$$

If the condition (5) holds for all the unit cells with an arbitrary pair of directions in a certain space, then this space belongs to the *perfect workspace* of the conformal IRS. For instance, the perfect workspace of a CyA with $\{\phi_{\text{lb}}, \phi_{\text{ub}}, d_{\text{v}}\} = \{-\frac{\pi}{6}, \frac{\pi}{6}, \frac{\lambda_c}{4}\}$ is $\{\phi \in [-\frac{\pi}{3}, \frac{\pi}{3}], \theta \in [0, \pi]\}$, while that of a SA with $\{\phi_{\text{lb}}, \phi_{\text{ub}}, \theta_{\text{lb}}, \theta_{\text{ub}}\} = \{-\pi, \pi, 0, \frac{\pi}{6}\}$ is $\{\phi \in [-\pi, \pi], \theta \in [0, \frac{\pi}{3}]\}$. By increasing the curvature radius or the array size of conformal IRSs, one can effectively reduce the occurrence probability of shadow effect to sustain an acceptable communication quality. Note that with sufficient training measurements, the proposed channel estimation schemes can recover the cascaded IRS response vectors and detect the unit cells affected by the shadow effect.[3]

III. CHANNEL ESTIMATION WITH SUFFICIENT MEASUREMENTS

The training signals (1) across $P_{\text{tr}}Q_{\text{tr}}$ time slots in total can be concatenated as $\mathbf{Y}_k = [\mathbf{y}_{k,1,1}, \mathbf{y}_{k,1,2}, \dots, \mathbf{y}_{k,P_{\text{tr}},Q_{\text{tr}}}] \in \mathbb{C}^{M_{\text{tr}} \times P_{\text{tr}}Q_{\text{tr}}}$. It can be equivalently regarded as a matricization form of a third-order tensor as $\mathbf{Y}_k = \text{Matr}(\boldsymbol{\mathcal{Y}}_k; 1, [3, 2])$, where $\boldsymbol{\mathcal{Y}}_k \in \mathbb{C}^{M_{\text{tr}} \times Q_{\text{tr}} \times P_{\text{tr}}}$ fits the CP tensor model with a maximal *CP-rank* of N_{I} as

$$\boldsymbol{\mathcal{Y}}_k = \sum_{n=1}^{N_{\text{I}}} \mathbf{W}_k^H[\mathbf{H}_{\text{BI},k}]_{:,n} \circ \mathbf{F}_k^T[\mathbf{H}_{\text{IU},k}]_{n,:}^T \circ [\boldsymbol{\Psi}_k]_{:,n} + \boldsymbol{\mathcal{N}}_k$$

$$= \boldsymbol{\mathcal{I}}_{3,N_{\text{I}}} \times_1 \widetilde{\mathbf{H}}_{\text{BI},k} \times_2 \widetilde{\mathbf{H}}_{\text{IU},k} \times_3 \boldsymbol{\Psi}_k + \boldsymbol{\mathcal{N}}_k, \tag{6}$$

where $\mathbf{F}_k \triangleq [\mathbf{F}_{k,1}\mathbf{x}_{k,1}, \dots, \mathbf{F}_{k,Q_{\text{tr}}}\mathbf{x}_{k,Q_{\text{tr}}}] \in \mathbb{C}^{N_{\text{U}} \times Q_{\text{tr}}}$; $\widetilde{\mathbf{H}}_{\text{BI},k} \triangleq \mathbf{W}_k^H\mathbf{H}_{\text{BI},k} \in \mathbb{C}^{M_{\text{tr}} \times N_{\text{I}}}$ and $\widetilde{\mathbf{H}}_{\text{IU},k} \triangleq \mathbf{F}_k^T\mathbf{H}_{\text{IU},k}^T \in \mathbb{C}^{Q_{\text{tr}} \times N_{\text{I}}}$ denote the equivalent channels; $\boldsymbol{\mathcal{N}}_k \in \mathbb{C}^{M_{\text{tr}} \times Q_{\text{tr}} \times P_{\text{tr}}}$

---

[3]The diagnosis technique has been developed for IRS-aided system monitoring and maintenance, which can locate faulty reflecting elements and retrieve failure parameters [39]. Moreover, a transmissive-reflective IRS with transparent substrates has also been proposed, which can provide a full 360° coverage to eliminate the shadow effect [40].

is the noise tensor; $\mathcal{I}_{3,N_I} \in \{0,1\}^{N_I \times N_I \times N_I}$ denotes a third-order identity tensor that contains ones in its diagonal. Note that by column-wisely arranging $\{\widetilde{\mathbf{H}}_{\mathrm{BI},k}\}_{k=1}^{K_{\mathrm{tr}}}$, $\{\widetilde{\mathbf{H}}_{\mathrm{IU},k}\}_{k=1}^{K_{\mathrm{tr}}}$ and $\{\boldsymbol{\Psi}_k\}_{k=1}^{K_{\mathrm{tr}}}$, one can derive a multi-carrier signal tensor with a maximal rank of $K_{\mathrm{tr}}N_I$. This method, however, increases the number of tensor inner components, leading to higher computational complexity. Thus, we subcarrier-wisely process the received training signals unless otherwise stated.

Performing the channel estimation is now equivalent to solving a decomposition problem of (6). Traditionally, one could employ iterative decomposition methods, e.g., alternating least squares (ALS) and approximate message passing (AMP) [16], [19], to implement the channel separation. Note that (6) contains information of structural antenna/reflector arrays, as well as, spatially sparse propagation channels. By fully exploiting these data characteristics, we can develop more effective parameter-based channel estimation schemes.

A. Beamforming Design

Define $\mathbf{Y}_{k(1)} \triangleq \mathrm{Matr}(\boldsymbol{\mathcal{Y}}_k; 1, [3,2])$ as the mode-1 unfolding of $\boldsymbol{\mathcal{Y}}_k$, and compute its dominant left singular vectors $\mathbf{U}_k \in \mathbb{C}^{M_{\mathrm{tr}} \times L_{\mathrm{BI}}}$. The column subspace of $\mathbf{Y}_{k(1)}$ can be linearly spanned as $\mathbf{U}_k \mathbf{T}_k^{-1}$ with $\mathbf{T}_k \in \mathbb{C}^{L_{\mathrm{BI}} \times L_{\mathrm{BI}}}$ being a nonsingular matrix. Supposing $M_{\mathrm{tr}} \ll N_B$, we present two feasible beamforming strategies to recover $\{\phi_{\mathrm{B},\ell_t}, \theta_{\mathrm{B},\ell_t}\}$.

1) On-Off Scheme: One simple way is to activate a number of antennas equal to the quantity of measurements in a Kronecker product form $\mathbf{W}_k = \mathbf{W}_{\mathrm{h},k} \otimes \mathbf{W}_{\mathrm{v},k}$ with

$$\mathbf{W}_{\mathrm{h(v)},k} = \begin{bmatrix} \mathbf{I}_{M_{\mathrm{h(v)}}} & \mathbf{0}_{M_{\mathrm{h(v)}} \times (N_{\mathrm{B,h(v)}} - M_{\mathrm{h(v)}})} \end{bmatrix}^T, \quad (7)$$

where $N_{\mathrm{B,h(v)}}, M_{\mathrm{h(v)}}$ are the numbers of antennas and data streams across the horizontal (vertical) aperture, respectively. The rotational-invariance property in 2-D element space is preserved as

$$(\mathbf{J}_{\mathrm{h}_2} \otimes \mathbf{I}_{M_{\mathrm{v}}})\mathbf{U}_k\mathbf{T}_k^{-1} = (\mathbf{J}_{\mathrm{h}_1} \otimes \mathbf{I}_{M_{\mathrm{v}}})\mathbf{U}_k\mathbf{T}_k^{-1}\boldsymbol{\Upsilon}_{\mathrm{h}}, \quad (8a)$$
$$(\mathbf{I}_{M_{\mathrm{h}}} \otimes \mathbf{J}_{\mathrm{v}_2})\mathbf{U}_k\mathbf{T}_k^{-1} = (\mathbf{I}_{M_{\mathrm{h}}} \otimes \mathbf{J}_{\mathrm{v}_1})\mathbf{U}_k\mathbf{T}_k^{-1}\boldsymbol{\Upsilon}_{\mathrm{v}}, \quad (8b)$$

where $\boldsymbol{\Upsilon}_{\mathrm{h}}, \boldsymbol{\Upsilon}_{\mathrm{v}} \in \mathbb{C}^{L_{\mathrm{BI}} \times L_{\mathrm{BI}}}$ are diagonal matrices containing $\left\{\kappa_{\mathrm{h},\ell_t} \triangleq \frac{2\pi d_{\mathrm{B,h}}}{\lambda_{\mathrm{c}}} \sin\theta_{\mathrm{B},\ell_t} \sin\phi_{\mathrm{B},\ell_t}\right\}$ and $\left\{\kappa_{\mathrm{v},\ell_t} \triangleq \frac{2\pi d_{\mathrm{B,v}}}{\lambda_{\mathrm{c}}} \cos\theta_{\mathrm{B},\ell_t}\right\}$, respectively, with $d_{\mathrm{B,h(v)}}$ being the horizontal (vertical) spacing; $\mathbf{J}_{\mathrm{h1(v1)}}, \mathbf{J}_{\mathrm{h2(v2)}} \in \{0,1\}^{(M_{\mathrm{h(v)}}-1) \times M_{\mathrm{h(v)}}}$ drop the first and last vector entries, respectively. Evidently, as the 2-D ESPRIT algorithm does, we can retrieve $\boldsymbol{\Upsilon}_{\mathrm{h(v)}}$ and $\mathbf{T}_k$ by performing an eigenvalue decomposition (EVD) on (8) under a LS criterion [41]. Note that the *simultaneous diagonalization* can be applied to automatically pair $\{\kappa_{\mathrm{h},\ell_t}\}$ and $\{\kappa_{\mathrm{v},\ell_t}\}$, from which $\{\phi_{\mathrm{B},\ell_t}, \theta_{\mathrm{B},\ell_t}\}$ can be easily recovered [42].

2) DFT Scheme: In order to maximize the beamforming gain of antennas while preserving the structural information, we adopt a beamspace combining design as

$$\big[\mathbf{W}_{\mathrm{h(v)},k}\big]_{:,m_{\mathrm{h(v)}}} = \big[\mathbf{D}_{N_{\mathrm{Bh(v)}}}\big]_{:,\omega_{m_{\mathrm{h(v)}}}} e^{j\frac{N_{\mathrm{Bh(v)}}-1}{2}\frac{2\pi\left(\omega_{m_{\mathrm{h(v)}}}-1\right)}{N_{\mathrm{Bh(v)}}}}, \quad (9)$$

where $\mathbf{D}_{N_{\mathrm{Bh(v)}}} \in \mathbb{C}^{N_{\mathrm{Bh(v)}} \times N_{\mathrm{Bh(v)}}}$ is a discrete Fourier transform (DFT) matrix; $\left\{\omega_{m_{\mathrm{h(v)}}}\right\}_{m_{\mathrm{h(v)}}=1}^{M_{\mathrm{h(v)}}}$ denote the searching codewords forming $D_{\mathrm{h(v)}}$ sectors of interest (SoI), where each SoI contains at least two consecutive codewords. By following [43, Lemma 4], we define the selection matrices $\overline{\mathbf{J}}_{\mathrm{h1(v1)}}, \overline{\mathbf{J}}_{\mathrm{h2(v2)}} \in \mathbb{R}^{(M_{\mathrm{h(v)}} - D_{\mathrm{h(v)}}) \times M_{\mathrm{h(v)}}}$. The rotational-invariance property in the 2-D beamspace is then preserved as

$$(\overline{\mathbf{J}}_{\mathrm{h}_2} \otimes \mathbf{I}_{M_{\mathrm{v}}})\mathbf{U}_k\mathbf{T}_k^{-1} = (\overline{\mathbf{J}}_{\mathrm{h}_1} \otimes \mathbf{I}_{M_{\mathrm{v}}})\mathbf{U}_k\mathbf{T}_k^{-1}\overline{\boldsymbol{\Upsilon}}_{\mathrm{h}}, \quad (10a)$$
$$(\mathbf{I}_{M_{\mathrm{h}}} \otimes \overline{\mathbf{J}}_{\mathrm{v}_2})\mathbf{U}_k\mathbf{T}_k^{-1} = (\mathbf{I}_{M_{\mathrm{h}}} \otimes \overline{\mathbf{J}}_{\mathrm{v}_1})\mathbf{U}_k\mathbf{T}_k^{-1}\overline{\boldsymbol{\Upsilon}}_{\mathrm{v}}, \quad (10b)$$

where $\overline{\boldsymbol{\Upsilon}}_{\mathrm{h}}, \overline{\boldsymbol{\Upsilon}}_{\mathrm{v}} \in \mathbb{R}^{L_{\mathrm{BI}} \times L_{\mathrm{BI}}}$ contain $\{\tan(\kappa_{\mathrm{h},\ell_t}/2)\}$ and $\{\tan(\kappa_{\mathrm{v},\ell_t}/2)\}$ on their diagonals, respectively. Following the 2-D beamspace unitary ESPRIT, the automatic pairing of $\{\kappa_{\mathrm{h},\ell_t}\}$ and $\{\kappa_{\mathrm{v},\ell_t}\}$ can be facilitated by performing a composite EVD as [41], [43]

$$\begin{aligned}
\mathbf{T}_k^{-1}(\overline{\boldsymbol{\Upsilon}}_{\mathrm{h}} + j\overline{\boldsymbol{\Upsilon}}_{\mathrm{v}})\mathbf{T}_k \\
= ((\overline{\mathbf{J}}_{\mathrm{h}_1} \otimes \mathbf{I}_{M_{\mathrm{v}}})\mathbf{U}_k)^\dagger (\overline{\mathbf{J}}_{\mathrm{h}_2} \otimes \mathbf{I}_{M_{\mathrm{v}}})\mathbf{U}_k \\
+ j((\mathbf{I}_{M_{\mathrm{h}}} \otimes \overline{\mathbf{J}}_{\mathrm{v}_1})\mathbf{U}_k)^\dagger (\mathbf{I}_{M_{\mathrm{h}}} \otimes \overline{\mathbf{J}}_{\mathrm{v}_2})\mathbf{U}_k. \quad (11)
\end{aligned}$$

Remark 2: For the case of precoding, one can similarly define $\mathbf{Y}_{k(2)} \triangleq \mathrm{Matr}(\boldsymbol{\mathcal{Y}}_k; 2, [3,1])$ and follow (8)–(11) to recover $\{\phi_{\mathrm{U},\ell_r}, \theta_{\mathrm{U},\ell_r}\}$. The structural properties of $\mathbf{W}_k^H \mathbf{a}_{\mathrm{B}}(\cdot)$ and $\mathbf{F}_k^T \mathbf{a}_{\mathrm{U}}^*(\cdot)$ are retained in the linear spans of $\mathbf{Y}_{k(1)}$ and $\mathbf{Y}_{k(2)}$, respectively. Generally, the rank of $\mathbf{Y}_{k(1)}$ or $\mathbf{Y}_{k(2)}$ equals to $\min(P_{\mathrm{tr}}\min(L_{\mathrm{BI}}, L_{\mathrm{IU}}), \max(L_{\mathrm{BI}}, L_{\mathrm{IU}}))$, leading to a feasibility condition for the parameter recovery $P_{\mathrm{tr}} \geq \left\lceil \frac{\max(L_{\mathrm{BI}}, L_{\mathrm{IU}})}{\min(L_{\mathrm{BI}}, L_{\mathrm{IU}})} \right\rceil$.

B. Parameter Recovery and Decoupling

After retrieving $\{\phi(\theta)_{\mathrm{B},\ell_t}, \phi(\theta)_{\mathrm{U},\ell_r}\}$, we remove their contributions, i.e., $\mathbf{A}_{\mathrm{B(U)}}$, from $\boldsymbol{\mathcal{Y}}_k$ by performing mode-1 and mode-2 *tensor-matrix products* (in the noiseless case) as

$$\begin{aligned}
\boldsymbol{\mathcal{Z}}_k &= \boldsymbol{\mathcal{Y}}_k \times_1 (\mathbf{W}_k^H \mathbf{A}_{\mathrm{B}})^\dagger \times_2 (\mathbf{F}_k^T \mathbf{A}_{\mathrm{U}}^*)^\dagger \\
&= \mathcal{I}_{3,N_I} \times_1 \mathrm{Diag}(\boldsymbol{\beta}_{\mathrm{BI},k})\mathbf{A}_{\mathrm{t}}^H \times_2 \mathrm{Diag}(\boldsymbol{\beta}_{\mathrm{IU},k})\mathbf{A}_{\mathrm{r}}^T \times_3 \boldsymbol{\Psi}_k.
\end{aligned} \quad (12)$$

The training pattern $\boldsymbol{\Psi}_k$ commonly has a rank of $\min(P_{\mathrm{tr}}, N_I)$. Given sufficient training measurements, i.e., $P_{\mathrm{tr}} \geq N_I$, we leverage the algebraic LS solution to derive in total $L \triangleq L_{\mathrm{BI}}L_{\mathrm{IU}}$ pairs of *cascaded* response vectors of the IRS array:

$$\begin{aligned}
\mathbf{G}_k &\triangleq \mathrm{Matr}\big(\boldsymbol{\mathcal{Z}}_k \times_3 \boldsymbol{\Psi}_k^\dagger; [2,1], 3\big) \\
&= \big(\mathrm{Diag}(\boldsymbol{\beta}_{\mathrm{BI},k}) \otimes \mathrm{Diag}(\boldsymbol{\beta}_{\mathrm{IU},k})\big)\big(\mathbf{A}_{\mathrm{t}}^H \odot \mathbf{A}_{\mathrm{r}}^T\big),
\end{aligned} \quad (13a)$$

$$[\mathbf{G}_k]_{\ell,:}^T = \beta_{\mathrm{BI},k,\ell_t}\beta_{\mathrm{IU},k,\ell_r} \underbrace{\mathbf{a}_{\mathrm{I}}^*(\phi_{\mathrm{t},\ell_t}, \theta_{\mathrm{t},\ell_t}) \circledast \mathbf{a}_{\mathrm{I}}(\phi_{\mathrm{r},\ell_r}, \theta_{\mathrm{r},\ell_r})}_{\mathbf{a}_{\mathrm{I,cas},\ell} \in \mathbb{C}^{N_I}}, \quad (13b)$$

where $\ell \triangleq (\ell_t - 1)L_{\mathrm{IU}} + \ell_r$ indexes the corresponding equivalent paths. In order to eliminate the distortion of the unknown path gains, we define the scalar variables

$g_{k,\ell}^{(n_1,n_2)} \triangleq [\mathbf{G}_k]_{\ell,n_1}[\mathbf{G}_k]_{\ell,n_2}^{-1}$, $n_1 < n_2 \in \mathcal{I}(N_\mathrm{I})$, whose amplitude and phase terms are respectively expressed as

$$\left| g_{k,\ell}^{(n_1,n_2)} \right|$$
$$= \left(\frac{f_+(\boldsymbol{\nu}_{n_1}^T \mathbf{d}(\phi_{\mathrm{t},\ell_\mathrm{t}}, \theta_{\mathrm{t},\ell_\mathrm{t}})) f_+(\boldsymbol{\nu}_{n_1}^T \mathbf{d}(\phi_{\mathrm{r},\ell_\mathrm{r}}, \theta_{\mathrm{r},\ell_\mathrm{r}}))}{f_+(\boldsymbol{\nu}_{n_2}^T \mathbf{d}(\phi_{\mathrm{t},\ell_\mathrm{t}}, \theta_{\mathrm{t},\ell_\mathrm{t}})) f_+(\boldsymbol{\nu}_{n_2}^T \mathbf{d}(\phi_{\mathrm{r},\ell_\mathrm{r}}, \theta_{\mathrm{r},\ell_\mathrm{r}}))} \right)^{\frac{\epsilon}{2}}, \tag{14a}$$

$$\angle g_{k,\ell}^{(n_1,n_2)}$$
$$= \frac{2\pi}{\lambda_\mathrm{c}} \left(\boldsymbol{\mu}_{n_1} - \boldsymbol{\mu}_{n_2} \right)^T \left(\mathbf{d}(\phi_{\mathrm{r},\ell_\mathrm{r}}, \theta_{\mathrm{r},\ell_\mathrm{r}}) - \mathbf{d}(\phi_{\mathrm{t},\ell_\mathrm{t}}, \theta_{\mathrm{t},\ell_\mathrm{t}}) \right). \tag{14b}$$

We construct $\mathbf{R} \in \mathbb{R}^{C_{N_\mathrm{I}}^2 \times 3}$ and $\mathbf{g}_{k,\ell} \in \mathbb{C}^{C_{N_\mathrm{I}}^2}$ by row-wisely concatenating $\{\boldsymbol{\mu}_{n_1}^T - \boldsymbol{\mu}_{n_2}^T\}$ and $\{g_{k,\ell}^{(n_1,n_2)}\}$, respectively, forming a linear system of equations. Note that there may exist a periodic ambiguity, i.e., $\arg(g_{k,\ell}^{(n_1,n_2)}) = \angle g_{k,\ell}^{(n_1,n_2)} + 2i\pi, i \in \mathbb{Z}$, referred to as a *spatial aliasing* or *phase wrapping* problem [44]. Since $\|\mathbf{d}(\phi_{\mathrm{r},\ell_\mathrm{r}}, \theta_{\mathrm{r},\ell_\mathrm{r}}) - \mathbf{d}(\phi_{\mathrm{t},\ell_\mathrm{t}}, \theta_{\mathrm{t},\ell_\mathrm{t}})\|_2 \leq 2$, we select $\mathcal{D} \triangleq \{(n_1,n_2) | \|\boldsymbol{\mu}_{n_1} - \boldsymbol{\mu}_{n_2}\|_2 \leq \lambda_\mathrm{c}/4\}$ to eliminate spatial aliasing. By introducing a diagonal weighting matrix $\mathbf{D} \in \mathbb{R}^{C_{N_\mathrm{I}}^2 \times C_{N_\mathrm{I}}^2}$ with $|\mathcal{D}|$ ones corresponding to the index tuples in $\mathcal{D}$, we apply a weighted least squares (WLS) solution to retrieve the *cascaded* phase parameters as

$$\underbrace{\begin{bmatrix} \omega_{\mathrm{x},\ell} \\ \omega_{\mathrm{y},\ell} \\ \omega_{\mathrm{z},\ell} \end{bmatrix}}_{\boldsymbol{\omega}_\ell \in \mathbb{R}^3} \triangleq \underbrace{\begin{bmatrix} \cos\phi_{\mathrm{r},\ell_\mathrm{r}} \sin\theta_{\mathrm{r},\ell_\mathrm{r}} - \cos\phi_{\mathrm{t},\ell_\mathrm{t}} \sin\theta_{\mathrm{t},\ell_\mathrm{t}} \\ \sin\phi_{\mathrm{r},\ell_\mathrm{r}} \sin\theta_{\mathrm{r},\ell_\mathrm{r}} - \sin\phi_{\mathrm{t},\ell_\mathrm{t}} \sin\theta_{\mathrm{t},\ell_\mathrm{t}} \\ \cos\theta_{\mathrm{r},\ell_\mathrm{r}} - \cos\theta_{\mathrm{t},\ell_\mathrm{t}} \end{bmatrix}}_{\mathbf{d}(\phi_{\mathrm{r},\ell_\mathrm{r}}, \theta_{\mathrm{r},\ell_\mathrm{r}}) - \mathbf{d}(\phi_{\mathrm{t},\ell_\mathrm{t}}, \theta_{\mathrm{t},\ell_\mathrm{t}})}$$
$$= \frac{\lambda_\mathrm{c}}{2\pi}(\mathbf{DR})^\dagger \mathbf{D} \arg(\mathbf{g}_{k,\ell}). \tag{15}$$

Generally, $\mathbf{R}$ has full column rank with $|\mathcal{D}| \gg 3$ that ensures the feasibility and uniqueness of (15). The spatial aliasing of $\arg(g_{k,\ell}^{(n_1,n_2)})$, $(n_1,n_2) \notin \mathcal{D}$ can be effectively corrected if a desirable initial estimate is available. Hence, to fully leverage the available training data, we adopt an iterative informed phase unwrapping (IPU) method [45]:

$$\angle \mathbf{g}_{k,\ell}^{(i)} = \arg(\mathbf{g}_{k,\ell}) - 2\pi \left\lfloor \frac{\arg(\mathbf{g}_{k,\ell}) - \frac{2\pi}{\lambda_\mathrm{c}} \mathbf{R} \boldsymbol{\omega}_\ell^{(i-1)} + \pi}{2\pi} \right\rfloor, \tag{16a}$$

$$\boldsymbol{\omega}_\ell^{(i)} = \frac{\lambda_\mathrm{c}}{2\pi} \mathbf{R}^\dagger \angle \mathbf{g}_{k,\ell}^{(i)}, \tag{16b}$$

where $\angle \mathbf{g}_{k,\ell}^{(i)}$, $\boldsymbol{\omega}_\ell^{(i)}$ denote the estimates of phase differences and cascaded angles at the ith iteration, respectively; the initial $\boldsymbol{\omega}_\ell^{(0)}$ is derived from the WLS method of (15). Since the observed phase differences are corrected by the addition of integer multiples of 2π, the convergence of (16) can be expected after a few iterations.

1) "All" Decoupling Mode: On each orthogonal direction, $L_\mathrm{BI} L_\mathrm{IU}$ equations with respect to the angular variables, i.e., $\cos\phi_{\mathrm{t(r)},\ell_\mathrm{t(r)}} \sin\theta_{\mathrm{t(r)},\ell_\mathrm{t(r)}}$, $\sin\phi_{\mathrm{t(r)},\ell_\mathrm{t(r)}} \sin\theta_{\mathrm{t(r)},\ell_\mathrm{t(r)}}$ and $\cos\theta_{\mathrm{t(r)},\ell_\mathrm{t(r)}}$, can be formulated, but only $(L_\mathrm{BI} + L_\mathrm{IU} - 1)$ of them are linearly independent. Equivalently, we can formulate in total $3(L_\mathrm{BI} + L_\mathrm{IU} - 1)$ effective nonlinear trigonometric equations with respect to $2(L_\mathrm{BI} + L_\mathrm{IU})$ parameters $\{\phi_{\mathrm{t(r)},\ell_\mathrm{t(r)}}, \theta_{\mathrm{t(r)},\ell_\mathrm{t(r)}}\}$. As long as this nonlinear equation system is not underdetermined, i.e., the number of propagation

paths satisfies

$$3(L_\mathrm{BI} + L_\mathrm{IU} - 1) \geq 2(L_\mathrm{BI} + L_\mathrm{IU}) \Leftrightarrow L_\mathrm{BI} + L_\mathrm{IU} \geq 3, \tag{17}$$

it is possible to decouple **all** the L sets of cascaded parameters simultaneously and achieve exact parameter estimates. We adopt the Levenberg-Marquardt algorithm (LMA), a trust region approach synthesizing the steepest descent and Gaussian-Newton methods, to solve the decoupling problem [46]. Define $\mathbf{x}_{\phi,\theta} \in \mathbb{R}^{2(L_\mathrm{BI}+L_\mathrm{IU})}$ as the variable vector of $\{\phi_{\mathrm{t(r)},\ell_\mathrm{t(r)}}, \theta_{\mathrm{t(r)},\ell_\mathrm{t(r)}}\}$, and $\boldsymbol{\omega}(\mathbf{x}_{\phi,\theta}) : \mathbb{R}^{2(L_\mathrm{BI}+L_\mathrm{IU})} \mapsto \mathbb{R}^{3L_\mathrm{BI}L_\mathrm{IU}}$ as the mapping function of cascaded parameters in (15). By leveraging the first-order Taylor expansion and damping method, the LS minimization problem at each iteration of LMA can be constructed as

$$\min_{\Delta \mathbf{x}_{\phi,\theta}^{(i)}} \frac{1}{2} \left\| \mathbf{e}_\omega(\mathbf{x}_{\phi,\theta}^{(i-1)}) + \mathbf{J}_{\mathbf{e}_\omega}(\mathbf{x}_{\phi,\theta}^{(i-1)}) \Delta \mathbf{x}_{\phi,\theta}^{(i)} \right\|_2^2$$
$$+ \frac{1}{2}\zeta \left(\Delta \mathbf{x}_{\phi,\theta}^{(i)} \right)^T \Delta \mathbf{x}_{\phi,\theta}^{(i)}, \tag{18a}$$

$$\text{s.t. } \mathbf{e}_\omega(\mathbf{x}_{\phi,\theta}) \triangleq \boldsymbol{\omega}(\mathbf{x}_{\phi,\theta}) - \hat{\boldsymbol{\omega}}, \; \mathbf{J}_{\mathbf{e}_\omega}(\mathbf{x}_{\phi,\theta}) \triangleq \frac{\partial \mathbf{e}_\omega(\mathbf{x}_{\phi,\theta})}{\partial \mathbf{x}_{\phi,\theta}}, \tag{18b}$$

where $\mathbf{x}_{\phi,\theta}^{(i)}, \Delta \mathbf{x}_{\phi,\theta}^{(i)} \in \mathbb{R}^{2(L_\mathrm{BI}+L_\mathrm{IU})}$ are the current estimate and update step at the ith iteration, respectively; $\hat{\boldsymbol{\omega}} \in \mathbb{R}^{3L_\mathrm{BI}L_\mathrm{IU}}$ is the actual estimate of $\{\hat{\boldsymbol{\omega}}_\ell\}_{\ell=1}^{L_\mathrm{BI}L_\mathrm{IU}}$ derived by (16); ζ is a tunable damping factor. The Jacobian matrix $\mathbf{J}_{\mathbf{e}_\omega}(\cdot) \in \mathbb{R}^{3L_\mathrm{BI}L_\mathrm{IU} \times 2(L_\mathrm{BI}+L_\mathrm{IU})}$ can be easily derived by exploiting the partial derivatives of $\mathbf{d}(\phi_{\mathrm{r},\ell_\mathrm{r}}, \theta_{\mathrm{r},\ell_\mathrm{r}}) - \mathbf{d}(\phi_{\mathrm{t},\ell_\mathrm{t}}, \theta_{\mathrm{t},\ell_\mathrm{t}})$ with respect to $\{\phi_{\mathrm{t(r)},\ell_\mathrm{t(r)}}, \theta_{\mathrm{t(r)},\ell_\mathrm{t(r)}}\}$. By computing the partial derivative of (18) with respect to $\Delta \mathbf{x}_{\phi,\theta}$ and setting it equal to zero, we can derive the *update normal equation* as

$$\left(\mathbf{J}_{\mathbf{e}_\omega}^T(\mathbf{x}_{\phi,\theta}^{(i-1)}) \mathbf{J}_{\mathbf{e}_\omega}(\mathbf{x}_{\phi,\theta}^{(i-1)}) + \zeta \mathbf{I}_{2(L_\mathrm{BI}+L_\mathrm{IU})} \right) \Delta \mathbf{x}_{\phi,\theta}^{(i)}$$
$$= -\mathbf{J}_{\mathbf{e}_\omega}^T(\mathbf{x}_{\phi,\theta}^{(i-1)}) \mathbf{e}_\omega(\mathbf{x}_{\phi,\theta}^{(i-1)}). \tag{19}$$

If the latest estimate $\mathbf{x}_{\phi,\theta}^{(i)} = \mathbf{x}_{\phi,\theta}^{(i-1)} + \Delta \mathbf{x}_{\phi,\theta}^{(i)}$ leads to a decreased objective error, we reduce ζ and increase the step size to accelerate the convergence; otherwise, we increase ζ and reject this update. For the specific rules of adjusting ζ, the interested readers are referred to [46, §4.1.1].

2) "Pair" Decoupling Mode: Note that if $L_\mathrm{BI} + L_\mathrm{IU} = 2$, i.e., $\mathbf{H}_{\mathrm{BI},k}$ and $\mathbf{H}_{\mathrm{IU},k}$ each contain only one single path (e.g., the LoS component), the LMA may not uniquely converge to the desired solution. In this case, we need to leverage the information of the angle-dependent power radiation pattern. For an arbitrary **pair** of $(\ell_\mathrm{t}, \ell_\mathrm{r})$, one can formulate a constrained multivariable LS minimization problem:[4]

$$\min_{\substack{\phi_{\mathrm{t},\ell_\mathrm{t}},\theta_{\mathrm{t},\ell_\mathrm{t}}, \\ \phi_{\mathrm{r},\ell_\mathrm{r}},\theta_{\mathrm{r},\ell_\mathrm{r}}}} \frac{1}{2}\|\mathbf{e}_{\mathbf{g},\ell}\|_2^2 \triangleq \frac{1}{2} \left\| \frac{\mathbf{g}_{\mathrm{I,cas},\ell}}{\|\mathbf{g}_{\mathrm{I,cas},\ell}\|_2} - \frac{\mathrm{abs}([\mathbf{G}_k]_{\ell,:}^T)}{\|[\mathbf{G}_k]_{\ell,:}^T\|_2} \right\|_2^2, \tag{20a}$$

$$\text{s.t. } \mathbf{d}(\phi_{\mathrm{r},\ell_\mathrm{r}}, \theta_{\mathrm{r},\ell_\mathrm{r}}) - \mathbf{d}(\phi_{\mathrm{t},\ell_\mathrm{t}}, \theta_{\mathrm{t},\ell_\mathrm{t}}) = \hat{\boldsymbol{\omega}}_\ell, \tag{20b}$$

[4]Based on (13), one can also straightforwardly utilize the amplitude equations $\left(\frac{[\mathbf{g}_{\mathrm{I,cas},\ell}]_{n_1}}{[\mathbf{g}_{\mathrm{I,cas},\ell}]_{n_2}} \right)^{\frac{\epsilon}{2}} = |g_{k,\ell}^{(n_1,n_2)}|, \forall n_1, n_2$ to formulate the minimization objective in (20), which involves no normalization operation.

where $\mathbf{g}_{\mathrm{I,cas},\ell} \triangleq \mathbf{g}_{\mathrm{I}}(\phi_{\mathrm{t},\ell_{\mathrm{t}}}, \theta_{\mathrm{t},\ell_{\mathrm{t}}}) \circledast \mathbf{g}_{\mathrm{I}}(\phi_{\mathrm{r},\ell_{\mathrm{r}}}, \theta_{\mathrm{r},\ell_{\mathrm{r}}})$ is the *cascaded* radiation pattern; the operations $\mathrm{abs}(\mathbf{a})$ and $\mathbf{a}/\|\mathbf{a}\|_2$ remove the phase and amplitude distortions of $\{\beta_{\mathrm{BI},k,\ell_{\mathrm{t}}}, \beta_{\mathrm{IU},k,\ell_{\mathrm{r}}}\}$, respectively. Instead of considering the scalar objective function $\frac{1}{2}\|\mathbf{e}_{\mathrm{g},\ell}\|_2^2$, we utilize each entry of $\mathbf{e}_{\mathrm{g},\ell} \in \mathbb{R}^{N_{\mathrm{I}}}$ to formulate up to N_{I} amplitude equations, along with three cascaded phase equations (20b), with respect to four variables. Based on the first-order derivatives presented in Appendix A, the LMA can be directly employed to solve (20).

After reconstructing the IRS response vectors, i.e., $\widehat{\mathbf{A}}_{\mathrm{t(r)}}$, through the decoupled angular parameters, the *cascaded* equivalent path gains, as well as, the *cascaded* time delays can be sequentially derived as

$$\rho_{\mathrm{BIU},k,\ell} \triangleq \beta_{\mathrm{BI},k,\ell_{\mathrm{t}}} \beta_{\mathrm{IU},k,\ell_{\mathrm{r}}} = \mathbf{e}_{L,\ell}^T \mathbf{G}_k \left(\widehat{\mathbf{A}}_{\mathrm{t}}^H \odot \widehat{\mathbf{A}}_{\mathrm{r}}^T \right)^{\dagger} \mathbf{e}_{L,\ell}, \tag{21a}$$

$$\tau_{\mathrm{BIU},\ell} \triangleq \tau_{\mathrm{BI},\ell_{\mathrm{t}}} + \tau_{\mathrm{IU},\ell_{\mathrm{r}}} = -\frac{K}{2\pi(k_1 - k_2)f_{\mathrm{s}}} \arg\left(\frac{\rho_{\mathrm{BIU},k_1,\ell}}{\rho_{\mathrm{BIU},k_2,\ell}} \right), \tag{21b}$$

where $k_1, k_2 \in \mathcal{I}(K_{\mathrm{tr}})$. One can average (21b) among multiple training subcarriers to enhance the recovery accuracy. Note that if $2\pi(k_1 - k_2)f_{\mathrm{s}}\tau_{\mathrm{BIU},k}/K \geq 2\pi$, there may exist a *temporal aliasing*, i.e., $\hat{\tau}_{\mathrm{BIU},\ell} = \tau_{\mathrm{BIU},\ell} - \frac{iK}{(k_1-k_2)f_{\mathrm{s}}}, i \in \mathbb{Z}$. This implies that the system bandwidth and training subcarrier interval should be carefully configured.

Remark 3: Traditional IRSs regularly arrange reflectors along one or two orthogonal spatial directions, while only one third or two thirds of data of $\{\boldsymbol{\omega}_\ell\}_{\ell=1}^{L_{\mathrm{BI}}L_{\mathrm{IU}}}$ in (14) can be retrieved. If the local coordinate system of the IRS does not coincide with the global one, one can only achieve one or two linear combinations of cascaded parameters of each pair of paths $(\ell_{\mathrm{t}}, \ell_{\mathrm{r}})$. One can thus formulate up to $2(L_{\mathrm{BI}}+L_{\mathrm{IU}}-1)$ equations with respect to $2(L_{\mathrm{BI}} + L_{\mathrm{IU}})$ variables. Recalling that the scalar power radiation pattern commonly gets wrapped with the path gains, the objective (20a) is invalid with little effective information, i.e., $\left|g_{k,\ell}^{(n_1,n_2)}\right| \equiv 1, \forall n_1, n_2$. Hence, only underdetermined equation systems can be constructed with common IRS topologies, which cannot yield unique solutions of the channel parameters. As a consequence, most existing works are bound to estimate the cascaded channel parameters without further processing, which limits significantly the integration of IRSs into wireless services [14]–[20]. By contrast, the proposed 3-D IRS topology empowers exact channel parameter recovery, supporting more wireless applications, e.g., environment mapping, user localization, mobility tracking, etc.

IV. CHANNEL ESTIMATION WITH INSUFFICIENT MEASUREMENTS

When the quantity of measurements is less than the number of reflectors, i.e., $P_{\mathrm{tr}} < N_{\mathrm{I}}$, the structural information of the IRS topology is compressed by the training pattern. As $\boldsymbol{\Psi}_k^{\dagger} \boldsymbol{\Psi}_k \neq \mathbf{I}_{N_{\mathrm{I}}}$, one cannot utilize the LS solution (12) to derive $\mathbf{G}_k \in \mathbb{C}^{L_{\mathrm{BI}}L_{\mathrm{IU}} \times N_{\mathrm{I}}}$, as well as, the cascaded channel $\mathbf{H}_{\mathrm{cas},k} \triangleq \mathbf{H}_{\mathrm{BI},k} \odot \mathbf{H}_{\mathrm{IU},k}^T = (\mathbf{A}_{\mathrm{B}} \otimes \mathbf{A}_{\mathrm{U}}^*) \mathbf{G}_k$. In order to realize channel estimation and parameter recovery with limited training measurements, we seek to exploit the in-depth

physical and electromagnetic characteristics of the conformal IRS unit cells.

A. Single-Carrier Training

One straightforward idea is to reduce the number of activated reflectors during the training procedure. With the existing manufacturing technology of IRSs, it is hard to physically implement such controllable switching-on/off circuits [17]–[19]. An alternative method is to geometrically arrange the reflectors as a *sparse* array with a degree of freedom comparable to that of the full one [47]. However, both schemes may reduce the beamforming gain or coverage range of conformal IRSs, yielding a weaker transceiving signal strength. Therefore, we manage to recover the compressed channel information from a signal processing point of view.

1) CS Scheme: A simple approach is to apply the existing CS technique to retrieve the angular parameters from the compressed cascaded response vector $\boldsymbol{\Psi}_k \mathbf{a}_{\mathrm{I,cas},\ell}$. The main challenge is the design of the four-dimensional (4-D) code-book with respect to $\{\phi_{\mathrm{t(r)},\ell_{\mathrm{t(r)}}}, \theta_{\mathrm{t},\ell_{\mathrm{t(r)}}}\}$. In order to reduce the time and space complexity of CS algorithms, we leverage a hierarchical design that recursively narrows the search with increased resolution.

We define the search grids of azimuth and elevation angles as $S_{\mathrm{h}}, S_{\mathrm{v}}$, respectively. The search range of the initial layer is $\left([\phi_{\min}^{(0)}, \phi_{\max}^{(0)}] \times [\theta_{\min}^{(0)}, \theta_{\max}^{(0)}]\right)^2$, which is evenly divided into $(S_{\mathrm{h}} \times S_{\mathrm{v}})^2$ codewords as $\left(\{\phi_{s_{\mathrm{h}}}^{(0)}\} \times \{\theta_{s_{\mathrm{v}}}^{(0)}\}\right)^2$. After the CS algorithm returns the indices of the best matching code-words, i.e., $(s_{\mathrm{h,t(r)}}^{\star}, s_{\mathrm{v,t(r)}}^{\star})$, we update the search range of the next layer as

$$\phi_{\min,\mathrm{t(r)}}^{(1)} = \phi_{s_{\mathrm{h,t(r)}}^{\star}}^{(0)} - W_{\mathrm{h}}/2, \phi_{\max,\mathrm{t(r)}}^{(1)} = \phi_{s_{\mathrm{h,t(r)}}^{\star}}^{(0)} + W_{\mathrm{h}}/2, \tag{22a}$$

$$\theta_{\min,\mathrm{t(r)}}^{(1)} = \theta_{s_{\mathrm{v,t(r)}}^{\star}}^{(0)} - W_{\mathrm{v}}/2, \theta_{\max,\mathrm{t(r)}}^{(1)} = \theta_{s_{\mathrm{v,t(r)}}^{\star}}^{(0)} + W_{\mathrm{v}}/2, \tag{22b}$$

where $W_{\mathrm{h(v)}}$ denotes the horizontal (vertical) window length. Then, the division and selection of the desired codewords are similar to those at the last layer. Based on (22), the codebook resolution is increased by $S_{\mathrm{h(v)}}/W_{\mathrm{h(v)}}$ times per layer. The estimation procedure terminates when the parameter resolution reaches the predefined threshold.

2) Direct Scheme: The dynamically derived 4-D CS code-books may entail heavy storage burden to the signal processor, whose resolution also limits the estimation accuracy. Thus, we now develop a flexible approach that directly extracts the channel parameters from the cascaded IRS response vectors. This is applicable to arbitrary conformal IRSs with general training patterns. By exploiting the representation of $\boldsymbol{\mathcal{Z}}_k$ in (11), one can verify that

$$s_{k,\ell}^{(p_1,p_2)} \triangleq \frac{[\boldsymbol{\mathcal{Z}}_k]_{\ell_{\mathrm{t}},\ell_{\mathrm{r}},p_1}}{[\boldsymbol{\mathcal{Z}}_k]_{\ell_{\mathrm{t}},\ell_{\mathrm{r}},p_2}} = \frac{[\boldsymbol{\Psi}_k]_{p_1,:}\mathbf{a}_{\mathrm{I,cas},\ell}}{[\boldsymbol{\Psi}_k]_{p_2,:}\mathbf{a}_{\mathrm{I,cas},\ell}}, \tag{23a}$$

$$0 = \left([\boldsymbol{\Psi}_k]_{p_1,:} - s_{k,\ell}^{(p_1,p_2)}[\boldsymbol{\Psi}_k]_{p_2,:}\right)\mathbf{a}_{\mathrm{I,cas},\ell}, \tag{23b}$$

where $p_1 < p_2 \in \mathcal{I}(P_{\mathrm{tr}})$. Define $\boldsymbol{\xi}_{k,\ell}^{(p_1,p_2)} \triangleq [\boldsymbol{\Psi}_k]_{p_1,:}^T - s_{k,\ell}^{(p_1,p_2)}[\boldsymbol{\Psi}_k]_{p_2,:}^T$, and row-wisely concatenate $\{\boldsymbol{\xi}_{k,\ell}^{(p_1,p_2)T}\}$ into

a matrix $\boldsymbol{\Xi}_{k,\ell} \in \mathbb{C}^{C_{P_{\mathrm{tr}}}^2 \times N_{\mathrm{I}}}$. We can now formulate a linear zero-forcing transformation, i.e., $\boldsymbol{\Xi}_{k,\ell} \mathbf{a}_{\mathrm{I},\mathrm{cas},\ell} = \mathbf{0}_{C_{P_{\mathrm{tr}}}^2}$. Note that the cascaded path gain $\rho_{\mathrm{BIU},k,\ell}$ has been eliminated via the division operation in (23). Then, the LS minimization problem with respect to the angular parameters of a pair of paths $(\ell_{\mathrm{t}}, \ell_{\mathrm{r}})$ can be constructed as

$$\min_{\phi_{\mathrm{t},\ell_{\mathrm{t}}}, \theta_{\mathrm{t},\ell_{\mathrm{t}}}, \phi_{\mathrm{r},\ell_{\mathrm{r}}}, \theta_{\mathrm{r},\ell_{\mathrm{r}}}} \frac{1}{2} \left\| \boldsymbol{\Xi}_{k,\ell} \left(\mathbf{g}_{\mathrm{I},\mathrm{cas},\ell} \circledast \mathbf{p}_{\mathrm{I},\mathrm{cas},\ell} \right) \right\|_2^2, \quad (24a)$$

$$\text{s.t. } \mathbf{g}_{\mathrm{I},\mathrm{cas},\ell} \triangleq \mathbf{g}_{\mathrm{I}}(\phi_{\mathrm{t},\ell_{\mathrm{t}}}, \theta_{\mathrm{t},\ell_{\mathrm{t}}}) \circledast \mathbf{g}_{\mathrm{I}}(\phi_{\mathrm{r},\ell_{\mathrm{r}}}, \theta_{\mathrm{r},\ell_{\mathrm{r}}}), \quad (24b)$$

$$\mathbf{p}_{\mathrm{I},\mathrm{cas},\ell} \triangleq \mathbf{p}_{\mathrm{I}}^*(\phi_{\mathrm{t},\ell_{\mathrm{t}}}, \theta_{\mathrm{t},\ell_{\mathrm{t}}}) \circledast \mathbf{p}_{\mathrm{I}}(\phi_{\mathrm{r},\ell_{\mathrm{r}}}, \theta_{\mathrm{r},\ell_{\mathrm{r}}}). \quad (24c)$$

The LMA can be applied to solve (24), which, however, may return complex-valued estimates due to the complex operations involved in the objective and constraints. Hence, we equivalently transform (24) into a real-valued optimization problem as follows:

$$\min_{\substack{\phi_{\mathrm{t},\ell_{\mathrm{t}}}, \theta_{\mathrm{t},\ell_{\mathrm{t}}}, \\ \phi_{\mathrm{r},\ell_{\mathrm{r}}}, \theta_{\mathrm{r},\ell_{\mathrm{r}}}}} \frac{1}{2} \left\| \begin{bmatrix} \Re(\boldsymbol{\Xi}_{k,\ell}) & -\Im(\boldsymbol{\Xi}_{k,\ell}) \\ \Im(\boldsymbol{\Xi}_{k,\ell}) & \Re(\boldsymbol{\Xi}_{k,\ell}) \end{bmatrix} \right.$$

$$\left. \begin{bmatrix} \mathbf{g}_{\mathrm{I},\mathrm{cas},\ell} \circledast \cos \boldsymbol{\gamma}_{\mathrm{I},\mathrm{cas},\ell} \\ \mathbf{g}_{\mathrm{I},\mathrm{cas},\ell} \circledast \sin \boldsymbol{\gamma}_{\mathrm{I},\mathrm{cas},\ell} \end{bmatrix} \right\|_2^2, \quad (25a)$$

$$\text{s.t. } [\mathbf{g}_{\mathrm{I},\mathrm{cas},\ell}]_n = f_+^{\frac{\epsilon}{2}} (\boldsymbol{\nu}_n^T \mathbf{d}(\phi_{\mathrm{t},\ell_{\mathrm{t}}}, \theta_{\mathrm{t},\ell_{\mathrm{t}}}))$$

$$\times f_+^{\frac{\epsilon}{2}} (\boldsymbol{\nu}_n^T \mathbf{d}(\phi_{\mathrm{r},\ell_{\mathrm{r}}}, \theta_{\mathrm{r},\ell_{\mathrm{r}}})), \quad (25b)$$

$$[\boldsymbol{\gamma}_{\mathrm{I},\mathrm{cas},\ell}]_n = \frac{2\pi}{\lambda_{\mathrm{c}}} \boldsymbol{\mu}_n^T (\mathbf{d}(\phi_{\mathrm{r},\ell_{\mathrm{r}}}, \theta_{\mathrm{r},\ell_{\mathrm{r}}}) - \mathbf{d}(\phi_{\mathrm{t},\ell_{\mathrm{t}}}, \theta_{\mathrm{t},\ell_{\mathrm{t}}})), \quad (25c)$$

where $\boldsymbol{\gamma}_{\mathrm{I},\mathrm{cas},\ell} \triangleq \angle \mathbf{p}_{\mathrm{I},\mathrm{cas},\ell} \in \mathbb{R}^{N_{\mathrm{I}}}$. Since (25) does not directly impose any constraint on the variables $\{\phi_{\mathrm{t(r)},\ell_{\mathrm{t(r)}}}, \theta_{\mathrm{t(r)},\ell_{\mathrm{t(r)}}}\}$ as in (18), the algorithm results are extremely sensitive to the initial point. To this end, we adopt the *particle swarm optimization (PSO)*, a population based stochastic optimization technique, to obtain an appropriate start point [48]. The algorithm is initialized with a population of random solutions, called particles, and searches for optima by updating generations. By keeping track of the current individual fitness and globally shared optima, the particles dynamically adjust their coordinates and velocities.

B. Multi-Carrier Training

We notice that the reflecting coefficients of the practical IRS unit cells vary with the frequencies of incident signals, causing a *dual phase- and amplitude-squint* effect that may undermine some applications, e.g., beamforming design and capacity optimization, in wideband systems [30]. This frequency-sensitive nature can also introduce additional information that supports our design of more effective channel estimation schemes.

1) Direct Scheme: Define $\boldsymbol{\mathcal{Y}} \in \mathbb{C}^{M_{\mathrm{tr}} \times Q_{\mathrm{tr}} \times P_{\mathrm{tr}} \times K_{\mathrm{tr}}}$ as the multi-carrier training signal that arranges $\{\boldsymbol{\mathcal{Y}}_k\}_{k=1}^{K_{\mathrm{tr}}}$ along its fourth dimension. In the same way, one can obtain the compressed wideband signal tensor $\boldsymbol{\mathcal{Z}} \in \mathbb{C}^{L_{\mathrm{BI}} \times L_{\mathrm{IU}} \times P_{\mathrm{tr}} \times K_{\mathrm{tr}}}$ as a concatenation of $\{\boldsymbol{\mathcal{Z}}_k\}_{k=1}^{K_{\mathrm{tr}}}$. One can verify

$$\mathbf{z}_\ell \triangleq [\mathrm{Matr}(\boldsymbol{\mathcal{Z}}; [3, 4], [2, 1])]_{:, (\ell_{\mathrm{t}} - 1)L_{\mathrm{IU}} + \ell_{\mathrm{r}}}$$

$$= \alpha_{\mathrm{BI},\ell_{\mathrm{t}}} \alpha_{\mathrm{IU},\ell_{\mathrm{r}}} \underbrace{\left[\varpi_{1,\ell} \boldsymbol{\Psi}_1^T, \ldots, \varpi_{K_{\mathrm{tr}},\ell} \boldsymbol{\Psi}_{K_{\mathrm{tr}}}^T \right]^T}_{\widetilde{\boldsymbol{\Psi}}_\ell \in \mathbb{C}^{K_{\mathrm{tr}} P_{\mathrm{tr}} \times N_{\mathrm{I}}}} \mathbf{a}_{\mathrm{I},\mathrm{cas},\ell},$$

$$(26)$$

where $\varpi_{k,\ell} \triangleq e^{-j\frac{2\pi k f_{\mathrm{s}}}{K} \tau_{\mathrm{BIU},\ell}}$. In the generic case,[5] since the dual phase- and amplitude-squint effect of IRSs is modeled as a continuous function [30, Eq. (1)–(3)], the phase-shifted wideband IRS training pattern $\widetilde{\boldsymbol{\Psi}}_\ell$ has a rank of $\min(K_{\mathrm{tr}} P_{\mathrm{tr}}, N_{\mathrm{I}})$. Assuming sufficient training subcarriers, i.e., $K_{\mathrm{tr}} \geq \lceil N_{\mathrm{I}}/P_{\mathrm{tr}} \rceil$, one can derive the LS solution of $\{\mathbf{a}_{\mathrm{I},\mathrm{cas},\ell}\}$ up to scalar scaling ambiguities. However, $\widetilde{\boldsymbol{\Psi}}_\ell$ is commonly undetermined due to the unknown $\{\varpi_{k,\ell}\}_{k=1}^{K_{\mathrm{tr}}}$. We thus formulate an optimization problem with respect to five variables $\{\phi_{\mathrm{t},\ell_{\mathrm{t}}}, \theta_{\mathrm{t},\ell_{\mathrm{t}}}, \phi_{\mathrm{r},\ell_{\mathrm{r}}}, \theta_{\mathrm{r},\ell_{\mathrm{r}}}, \tau_{\mathrm{BIU},\ell}\}$ as

$$\min_{\substack{\phi_{\mathrm{t},\ell_{\mathrm{t}}}, \theta_{\mathrm{t},\ell_{\mathrm{t}}}, \\ \phi_{\mathrm{r},\ell_{\mathrm{r}}}, \theta_{\mathrm{r},\ell_{\mathrm{r}}}, \\ \tau_{\mathrm{BIU},\ell}}} \frac{1}{2} \left\| \frac{\mathbf{g}_{\mathrm{I},\mathrm{cas},\ell}}{\|\mathbf{g}_{\mathrm{I},\mathrm{cas},\ell}\|_2} - \frac{\mathrm{abs}\left(\widetilde{\boldsymbol{\Psi}}^\dagger(\boldsymbol{\varpi}_\ell) \mathbf{z}_\ell \right)}{\left\| \widetilde{\boldsymbol{\Psi}}^\dagger(\boldsymbol{\varpi}_\ell) \mathbf{z}_\ell \right\|_2} \right\|_2^2 \quad (27a)$$

$$\text{s.t. } \mathbf{d}(\phi_{\mathrm{r},\ell_{\mathrm{r}}}, \theta_{\mathrm{r},\ell_{\mathrm{r}}}) - \mathbf{d}(\phi_{\mathrm{t},\ell_{\mathrm{t}}}, \theta_{\mathrm{t},\ell_{\mathrm{t}}})$$

$$= \frac{\lambda_{\mathrm{c}}}{2\pi} (\mathbf{D}\mathbf{R})^\dagger \mathbf{D} \arg\left(\widetilde{\boldsymbol{\Psi}}^\dagger(\boldsymbol{\varpi}_\ell) \mathbf{z}_\ell \right), \quad (27b)$$

$$\widetilde{\boldsymbol{\Psi}}(\boldsymbol{\varpi}_\ell) \triangleq \left[\varpi_{1,\ell} \boldsymbol{\Psi}_1^T, \ldots, \varpi_{K_{\mathrm{tr}},\ell} \boldsymbol{\Psi}_{K_{\mathrm{tr}}}^T \right]^T, \quad (27c)$$

where $\boldsymbol{\varpi}_\ell \triangleq [\varpi_{1,\ell}, \ldots, \varpi_{K_{\mathrm{tr}},\ell}]^T$; $\mathbf{D} \in \mathbb{R}^{C_{N_{\mathrm{I}}}^2 \times C_{N_{\mathrm{I}}}^2}$, $\mathbf{R} \in \mathbb{R}^{C_{N_{\mathrm{I}}}^2 \times 3}$ follow the idential definitions as in (14). This problem can also be converted into a real-valued version to prevent the LMA from converging to complex-valued estimates. Note that according to the feature scaling theory, the nanosecond-level time delays $\{\tau_{\mathrm{BIU},\ell}\}$ should be normalized, e.g., into the range $[0, 1]$, to accelerate the convergence of gradient-based algorithms.

In order to avoid dynamically calculating the derivatives with respect to $\widetilde{\boldsymbol{\Psi}}^\dagger(\boldsymbol{\varpi}_\ell)$, we here develop a hierarchical search strategy similar to (20). We define the initial search range of time delays $[\tau_{\min}^{(0)}, \tau_{\max}^{(0)}]$, which is uniformly divided into S_τ codewords $\{\tau_{s_\tau}^{(0)}\}$. Given one codeword and its corresponding phase-shifted multi-carrier IRS training pattern, one can directly utilize the aforementioned LS scheme combined with the All/Pair decoupling modes to recover the channel parameters in $\mathbf{a}_{\mathrm{I},\mathrm{cas},\ell}$. The best matching codeword index, i.e., $s_\tau^\star$, is chosen as the one that results in the smallest objective error $\frac{1}{2}\|\mathbf{e}_{\mathbf{g},\ell}\|_2^2$. Then, its neighbouring region $[\tau_{s_\tau^\star - W_\tau/2}^{(0)}, \tau_{s_\tau^\star + W_\tau/2}^{(0)}]$ is selected with a window length W_τ as the updated search range for the next layer. The wideband training pattern $\widetilde{\boldsymbol{\Psi}}(\cdot)$ with respect to the predefined codewords can be computed in advance and stored at the signal processing terminal.

2) Subspace Scheme: In order to further reduce the computational complexity in the case of large amounts of training subcarriers, we develop a more efficient algorithm by exploiting the frequency-sensitive characteristics of IRS training pattern. We recall that $\mathbf{a}_{\mathrm{I},\mathrm{cas},\ell}$ belongs to the kernel (nullspace)

---

[5]A generic property means that it holds with probability one when the values of the training pattern matrices are drawn from absolutely continuous probability density functions [30].

of $\boldsymbol{\Xi}_{k,\ell}$ in (21), (22); moreover, $\left\{\boldsymbol{\xi}_{k,\ell}^{(p_1,p_2)}\right\}$ generally construct a maximal linearly independent set of at most $(P_{\mathrm{tr}}-1)$ vectors, yielding $\mathrm{rank}(\boldsymbol{\Xi}_{k,\ell}) = P_{\mathrm{tr}} - 1$. According to the *rank-nullity theorem* [49, Eq. (3.205)], $\dim(\ker(\boldsymbol{\Xi}_{k,\ell})) = N_{\mathrm{I}} - P_{\mathrm{tr}} + 1$ with an orthogonal basis $\{\mathbf{b}_{k,\ell,1}, \ldots, \mathbf{b}_{k,\ell,N_{\mathrm{I}}-P_{\mathrm{tr}}}, \mathbf{a}_{\mathrm{I,cas},\ell}\} \in \mathbb{C}^{N_{\mathrm{I}}}$.

In the generic case, there exists a maximal linearly independent set of $\min(2(N_{\mathrm{I}} - P_{\mathrm{tr}}) + 1, N_{\mathrm{I}})$ vectors among $\left\{\{\mathbf{b}_{k_1,\ell,i}\}_{i=1}^{N_{\mathrm{I}}-P_{\mathrm{tr}}}, \{\mathbf{b}_{k_2,\ell,i}\}_{i=1}^{N_{\mathrm{I}}-P_{\mathrm{tr}}}, \mathbf{a}_{\mathrm{I,cas},\ell}\right\}$ for two subcarriers indexed by k_1, k_2. Thus, we have $\dim(\ker(\boldsymbol{\Xi}_{k_1,\ell}) + \ker(\boldsymbol{\Xi}_{k_2,\ell})) = \min(2(N_{\mathrm{I}} - P_{\mathrm{tr}}) + 1, N_{\mathrm{I}})$. Define $\boldsymbol{\Xi}_{k_1 k_2,\ell} \triangleq \left[\boldsymbol{\Xi}_{k_1,\ell}^T, \boldsymbol{\Xi}_{k_2,\ell}^T\right]^T$ that has a kernel as the intersection of the nullspaces, i.e., $\ker(\boldsymbol{\Xi}_{k_1,\ell}) \cap \ker(\boldsymbol{\Xi}_{k_2,\ell})$. The dimension of $\ker(\boldsymbol{\Xi}_{k_1 k_2,\ell})$ can be derived by the *dimension formula* as follows [49, Eq. (2.15)]:

$$\begin{aligned}
\dim(\ker(\boldsymbol{\Xi}_{k_1 k_2,\ell})) &= \dim(\ker(\boldsymbol{\Xi}_{k_1,\ell})) + \dim(\ker(\boldsymbol{\Xi}_{k_2,\ell})) \\
&\quad - \dim(\ker(\boldsymbol{\Xi}_{k_1,\ell}) + \ker(\boldsymbol{\Xi}_{k_2,\ell})) \\
&= 2(N_{\mathrm{I}} - P_{\mathrm{tr}} + 1) \\
&\quad - \min(2(N_{\mathrm{I}} - P_{\mathrm{tr}}) + 1, N_{\mathrm{I}}), \\
&= \max(1, N_{\mathrm{I}} - 2(P_{\mathrm{tr}} - 1)). \quad (28)
\end{aligned}$$

Furthermore, (28) can be extended to the case of K_{tr} training subcarriers. By concatenating the multi-carrier IRS training coefficients as $\boldsymbol{\Xi}_\ell \triangleq \left[\boldsymbol{\Xi}_{1,\ell}^T, \ldots, \boldsymbol{\Xi}_{K_{\mathrm{tr}},\ell}^T\right]^T \in \mathbb{C}^{K_{\mathrm{tr}} C_{P_{\mathrm{tr}}}^2 \times N_{\mathrm{I}}}$, we have

$$\mathrm{rank}(\boldsymbol{\Xi}_\ell) = \min(N_{\mathrm{I}} - 1, K_{\mathrm{tr}}(P_{\mathrm{tr}} - 1)), \quad (29\mathrm{a})$$

$$\dim(\ker(\boldsymbol{\Xi}_\ell)) = \max(1, N_{\mathrm{I}} - K_{\mathrm{tr}}(P_{\mathrm{tr}} - 1)). \quad (29\mathrm{b})$$

Obviously, given sufficient frequency resources, i.e., $K_{\mathrm{tr}} \geq \left\lceil \frac{N_{\mathrm{I}}-1}{P_{\mathrm{tr}}-1} \right\rceil$, $\boldsymbol{\Xi}_\ell$ has a rank-one kernel with a single basis vector $\mathbf{b}_{\ell,1} \in \mathbb{C}^{N_{\mathrm{I}}}$. According to (21), (29), the cascaded response vector coincidentally belongs to this kernel, i.e., $\boldsymbol{\Xi}_\ell \mathbf{a}_{\mathrm{I,cas},\ell} = \mathbf{0}_{K_{\mathrm{tr}} C_{P_{\mathrm{tr}}}^2}$, and thus can be uniquely represented by $\mathbf{b}_{\ell,1}$ up to a scalar scaling ambiguity. We develop a simple procedure to compute the kernel basis by exploiting the following property of kernel intersection:

Lemma 1 [50, Theorem 6.4.1]: Define the orthogonal basis for $\ker(\boldsymbol{\Xi}_{k_1,\ell})$ as $\mathbf{B}_{k_1,\ell} \triangleq [\mathbf{b}_{k_1,\ell,1}, \ldots, \mathbf{b}_{k_1,\ell,N_{\mathrm{I}}-P_{\mathrm{tr}}+1}]$. Define the orthogonal basis for $\ker(\boldsymbol{\Xi}_{k_2,\ell} \mathbf{B}_{k_1,\ell})$ as $\mathbf{V}_{k_1 k_2,\ell} \triangleq [\mathbf{v}_{k_1 k_2,\ell,1}, \ldots, \mathbf{v}_{k_1 k_2,\ell,N_{\mathrm{I}}-2(P_{\mathrm{tr}}-1)}]$. Then, $\mathbf{B}_{k_1,\ell} \mathbf{V}_{k_1 k_2,\ell}$ forms an orthogonal basis for $\ker(\boldsymbol{\Xi}_{k_1,\ell}) \cap \ker(\boldsymbol{\Xi}_{k_2,\ell})$.

By recursively performing the operations of Lemma 1, one can gradually update the desired subspace from the multi-carrier IRS training patterns, i.e., calculating the basis of $\bigcap_{k=k_1}^{k_i} \ker(\boldsymbol{\Xi}_{k,\ell})$ at the ith iteration. Note that in practice, the environmental noise will interfere the direct derivation of kernel subspaces. We approximate the kernel basis of a matrix by its right singular vectors corresponding to the least singular values.

V. IRS-EMPOWERED ENVIRONMENT MAPPING

With precisely recovered channel parameters, many applications of environment mapping, e.g., scatterer positioning, user localization and orientation, etc., can be realized with high resolution. We assume that in the global coordinate system, the BS, UE and IRS are located at $\mathbf{p}_{\mathrm{B}}$, $\mathbf{p}_{\mathrm{U}}$ and $\mathbf{p}_{\mathrm{I}} \in \mathbb{R}^3$ with

orientations $\mathbf{n}_{\mathrm{B}}$, $\mathbf{n}_{\mathrm{U}}$ and $\mathbf{n}_{\mathrm{I}} \in \mathbb{R}^3$, respectively. For a linear or planar antenna array, its orientation is commonly set as the identical normal direction of elements; for a conformal reflector array, its orientation can be arbitrarily defined. Moreover, we define the *default orientations* of the BS, UE and IRS in their local coordinate systems as $\dot{\mathbf{n}}_{\mathrm{B}}$, $\dot{\mathbf{n}}_{\mathrm{U}}$ and $\dot{\mathbf{n}}_{\mathrm{I}} \in \mathbb{R}^3$, respectively.[6]

A. Environment Mapping

One significant step of environment mapping is to construct the relationship between the global and local coordinate systems, which determines the transformation of the communication channel parameters to physical geographic parameters. Generally, the rotation of a device with an actual orientation $\mathbf{n} = [n_{\mathrm{x}}, n_{\mathrm{y}}, n_{\mathrm{z}}]^T$ from a default one $\dot{\mathbf{n}} = [\dot{n}_{\mathrm{x}}, \dot{n}_{\mathrm{y}}, \dot{n}_{\mathrm{z}}]^T$ can be parameterized by a *rotation axis* and a *rotation angle* as

$$\mathbf{c} \triangleq \dot{\mathbf{n}} \times \mathbf{n} = \begin{bmatrix} c_{\mathrm{x}} \\ c_{\mathrm{y}} \\ c_{\mathrm{z}} \end{bmatrix} = \begin{bmatrix} \dot{n}_{\mathrm{y}} n_{\mathrm{z}} - \dot{n}_{\mathrm{z}} n_{\mathrm{y}} \\ \dot{n}_{\mathrm{z}} n_{\mathrm{x}} - \dot{n}_{\mathrm{x}} n_{\mathrm{z}} \\ \dot{n}_{\mathrm{x}} n_{\mathrm{y}} - \dot{n}_{\mathrm{y}} n_{\mathrm{x}} \end{bmatrix}, \quad (30\mathrm{a})$$

$$\xi \triangleq \arccos(\dot{\mathbf{n}} \bullet \mathbf{n}) = \arccos(\dot{n}_{\mathrm{x}} n_{\mathrm{x}} + \dot{n}_{\mathrm{y}} n_{\mathrm{y}} + \dot{n}_{\mathrm{z}} n_{\mathrm{z}}), \quad (30\mathrm{b})$$

where $\|\mathbf{c}\|_2 = \sin \xi$. This rotation can be realized by the *Rodrigues' rotation formula* as [51]

$$\mathbf{n} = \dot{\mathbf{n}} \cos \xi + \mathbf{c} \times \dot{\mathbf{n}} + \mathbf{c}(\mathbf{c} \bullet \dot{\mathbf{n}}) \frac{1 - \cos \xi}{\sin^2 \xi}. \quad (31)$$

Then, the rotation matrix for (31) can be derived as

$$\mathbf{R}_{\dot{\mathbf{n}} \to \mathbf{n}} \triangleq \mathbf{I}_3 + \mathbf{C} + \mathbf{C}^2 \frac{1 - \cos \xi}{\sin^2 \xi}, \quad (32\mathrm{a})$$

$$\mathbf{C} \triangleq \begin{bmatrix} 0 & -c_{\mathrm{z}} & c_{\mathrm{y}} \\ c_{\mathrm{z}} & 0 & -c_{\mathrm{x}} \\ -c_{\mathrm{y}} & c_{\mathrm{x}} & 0 \end{bmatrix}, \quad (32\mathrm{b})$$

where $(1 - \cos \xi)/\sin^2 \xi = (1 + \cos \xi)^{-1}$; $\mathbf{C} \in \mathbb{R}^{3 \times 3}$ is the cross-product matrix of $\mathbf{c}$. The linear transformation $\mathbf{n} = \mathbf{R}_{\dot{\mathbf{n}} \to \mathbf{n}} \dot{\mathbf{n}}$ is expressed explicitly in terms of the elements of $\{\dot{\mathbf{n}}, \mathbf{n}\}$. Given *a priori* device orientations, one can determine the rotation transformations of the BS and IRS, denoted by $\mathbf{R}_{\mathrm{B}}$ and $\mathbf{R}_{\mathrm{I}} \in \mathbb{C}^{3 \times 3}$ respectively. By substituting the recovered angular parameters into the unit direction function $\mathbf{d}(\phi, \theta)$, we derive the local directions of signal paths, i.e., $\dot{\mathbf{d}}_{\mathrm{B},\ell_{\mathrm{t}}}$, $\dot{\mathbf{d}}_{\mathrm{t},\ell_{\mathrm{t}}}$ and $\dot{\mathbf{d}}_{\mathrm{r},\ell_{\mathrm{r}}} \in \mathbb{R}^3$. Their corresponding global directions, denoted by $\mathbf{d}_{\mathrm{B},\ell_{\mathrm{t}}}$, $\mathbf{d}_{\mathrm{t},\ell_{\mathrm{t}}}$ and $\mathbf{d}_{\mathrm{r},\ell_{\mathrm{r}}} \in \mathbb{R}^3$, are then calculated as $\mathbf{d}_{\mathrm{B},\ell_{\mathrm{t}}} = \mathbf{R}_{\mathrm{B}} \dot{\mathbf{d}}_{\mathrm{B},\ell_{\mathrm{t}}}$, $\mathbf{d}_{\mathrm{t(r)},\ell_{\mathrm{t(r)}}} = \mathbf{R}_{\mathrm{I}} \dot{\mathbf{d}}_{\mathrm{t(r)},\ell_{\mathrm{t(r)}}}$.

We note that the orientation of the UE is commonly unknown, whose Rodrigues' rotation from $\dot{\mathbf{n}}_{\mathrm{U}}$ to $\mathbf{n}_{\mathrm{U}}$ cannot be uniquely recovered based on $\dot{\mathbf{d}}_{\mathrm{U},\ell_{\mathrm{r}}}, \mathbf{d}_{\mathrm{U},\ell_{\mathrm{r}}} \in \mathbb{R}^3$. To this end, we apply another definition of device rotation following an artificially specified procedure. The default orientation of the UE is set as $\dot{\mathbf{n}}_{\mathrm{U}} \triangleq [1, 0, 0]^T$, while the actual one is $\mathbf{n}_{\mathrm{U}} \triangleq \mathbf{d}(\phi_{\mathrm{U}}, \theta_{\mathrm{U}})$ defined by two *orientation angles* $\{\phi_{\mathrm{U}}, \theta_{\mathrm{U}}\}$.

---

[6]The default orientation mainly determines the specific expression form of array response vectors. For instance, for an UPA on the local x-y plane with a normal $[0, 0, 1]^T$, the unit phase shift terms along the array aperture are $\{\sin \theta \cos \phi, \sin \theta \sin \phi\}$; for an UPA on the local y-z plane with a normal $[1, 0, 0]^T$, the unit phase shift terms are $\{\sin \theta \sin \phi, \cos \theta\}$.

With the right-hand rule in mind, the rotation from $\dot{\mathbf{n}}_U$ to $\mathbf{n}_U$ is divided into one rotation by $(\theta_U - \pi/2)$ around the y-axis followed by another rotation by ϕ_U around the z-axis. Thus, the corresponding rotation matrix is given by

$$
\begin{aligned}
\mathbf{R}_U&(\phi_U, \theta_U) \\
&\triangleq \mathbf{R}_z(\phi_U)\mathbf{R}_y(\theta_U - \pi/2) \\
&= \begin{bmatrix}
\cos\phi_U \sin\theta_U & -\sin\phi_U & -\cos\phi_U \cos\theta_U \\
\sin\phi_U \sin\theta_U & \cos\phi_U & -\sin\phi_U \cos\theta_U \\
\cos\theta_U & 0 & \sin\theta_U
\end{bmatrix},
\end{aligned} \quad (33)
$$

where $\mathbf{R}_{y(z)}(\cdot) \in \mathbb{R}^{3\times3}$ denotes the basic yaw (pitch) rotation matrix. With specified rotation angles and axes, the rotation parameters of (33) are possible to be uniquely retrieved.

The scatterer located at $\mathbf{s}_{BI,\ell_t} \in \mathbb{R}^3$ is the intersection point of two spatial lines passing through $\mathbf{p}_B$ and $\mathbf{p}_I$ with directions $\mathbf{d}_{B,\ell_t}$ and $\mathbf{d}_{t,\ell_t}$, respectively. In practice, the estimated lines may not exactly intersect, and the median point of their common perpendicular can serve as an approximate estimate of the scatterer position. Denote two points by $\mathbf{q}_B(x_1) \triangleq \mathbf{p}_B + x_1\mathbf{d}_{B,\ell_t}$ and $\mathbf{q}_I(x_2) \triangleq \mathbf{p}_I + x_2\mathbf{d}_{t,\ell_t}$ with $x_1, x_2 \in \mathbb{R}$. Then, the scatterer coordinates can be derived as follows

$$
\min_{\mathbf{x} \triangleq [x_1, -x_2]^T} \|\mathbf{q}_B(x_1) - \mathbf{q}_I(x_2)\|_2^2 = \|\mathbf{Ax} - \mathbf{b}\|_2^2 \quad (34a)
$$

$$
\text{s.t. } \mathbf{A} \triangleq \begin{bmatrix} \mathbf{d}_{B,\ell_t} & \mathbf{d}_{t,\ell_t} \end{bmatrix}, \quad \mathbf{b} \triangleq \mathbf{p}_I - \mathbf{p}_B, \quad (34b)
$$

$$
\mathbf{s}_{BI,\ell_t} = \frac{1}{2}(\mathbf{q}_B(x_1^\star) + \mathbf{q}_I(x_2^\star)), \quad (34c)
$$

where $\{x_1^\star, x_2^\star\}$ is calculated by the LS solution of (34) as $\mathbf{x}^\star = (\mathbf{A}^T\mathbf{A})^{-1}\mathbf{A}^T\mathbf{b}$. Then, the time delay of the corresponding IRS-to-BS NLoS path is simply computed as

$$
\tau_{BI,\ell_t} = \frac{1}{v_c}(\|\mathbf{p}_B - \mathbf{s}_{BI,\ell_t}\|_2 + \|\mathbf{p}_I - \mathbf{s}_{BI,\ell_t}\|_2), \quad (35)
$$

where $v_c = 3 \times 10^8$ m/s is the light velocity. Given the estimate of the cascaded time delay $\tau_{BIU,\ell}$ in (19), one can directly recover the time delay of the corresponding UE-to-IRS path as $\tau_{IU,\ell_r} = \tau_{BIU,\ell} - \tau_{BI,\ell_t}$.

B. User Localization and Orientation

We suppose that $\mathbf{H}_{IU,k}$ contains a LoS path indexed by $\ell_r = 1$, which can be identified by its smallest propagation delay. One can simply realize the user localization by utilizing a hybrid angle-delay positioning scheme:

$$
\mathbf{p}_U = \mathbf{p}_I + \mathbf{d}_{r,1}v_c\tau_{IU,1}. \quad (36)
$$

The global direction of the LoS path is $\mathbf{d}_{U,1} = -\mathbf{d}_{r,1} = (\mathbf{p}_I - \mathbf{p}_U)/v_c\tau_{IU,1}$, whilst the local one is $\dot{\mathbf{d}}_{U,1} = \mathbf{d}(\phi_{U,1}, \theta_{U,1})$ with the estimated AoDs $\{\phi_{U,1}, \theta_{U,1}\}$. These two direction vectors also follow the transformation $\mathbf{d}_{U,1} = \mathbf{R}(\phi_U, \theta_U)\dot{\mathbf{d}}_{U,1}$. By applying the *universal formulas of trigonometric functions* to the third row of (33), one can verify that

$$
[\dot{\mathbf{d}}_{U,1}]_1 \frac{1 - \vartheta_U^2}{1 + \vartheta_U^2} + [\dot{\mathbf{d}}_{U,1}]_3 \frac{2\vartheta_U}{1 + \vartheta_U^2} = [\mathbf{d}_{U,1}]_3, \quad (37)
$$

where $\vartheta_U \triangleq \tan(\theta_U/2)$. Clearly, there exist two solutions of ϑ_U to the quadratic equation (37). By substituting these two solutions back into the first two rows of (33), one can correspondingly derive two solutions of $\varphi_U \triangleq \tan(\phi_U/2)$. The incorrect solution of $\{\varphi_U, \vartheta_U\}$ can be immediately discarded only when it obviously falls outside the feasible region. In this case, the additional information from the NLoS components of $\mathbf{H}_{IU,k}$ is necessary to help obtaining the precise estimates of orientation angles. For the ith $(i \in \{1,2\})$ candidate $\{\phi_U^{(i)}, \theta_U^{(i)}\}$, the scatterers between the IRS and UE can be localized similarly as in (34):

$$
\begin{aligned}
\mathbf{s}_{IU,\ell_r} = &\frac{1}{2}\left(\begin{bmatrix} \mathbf{d}_{U,\ell_r}^{(i)} & -\mathbf{d}_{r,\ell_r} \end{bmatrix} \begin{bmatrix} \mathbf{d}_{U,\ell_r}^{(i)} & \mathbf{d}_{r,\ell_r} \end{bmatrix}^\dagger (\mathbf{p}_I - \mathbf{p}_U)\right) \\
&+ \frac{1}{2}(\mathbf{p}_U + \mathbf{p}_I),
\end{aligned} \quad (38)
$$

where $\mathbf{d}_{U,\ell_r}^{(i)} = \mathbf{R}_U(\phi_U^{(i)}, \theta_U^{(i)})\dot{\mathbf{d}}_{U,\ell_r}$. The corresponding time delay $\tau_{IU,\ell_r}^{(i)}$ is then computed. Recalling that the exact estimate of τ_{IU,ℓ_r} has been obtained by (35), the correct estimates of orientation can be determined as

$$
\mathbf{n}_U = \mathbf{d}(\phi_U^{(i^\star)}, \theta_U^{(i^\star)}), i^\star = \arg\min_{i \in \{1,2\}} |\tau_{IU,\ell_r}^{(i)} - \tau_{IU,\ell_r}|. \quad (39)
$$

VI. NUMERICAL RESULTS

The typical settings of simulation parameters are listed here: $N_I = 36 \ (6 \times 6)$, $N_B = N_U = 36 \ (6 \times 6)$, $M_{tr} = Q_{tr} = 16 \ (4 \times 4)$; $K = 128$, $f_s = 0.32$ GHz, $f_c = 28$ GHz; $L_{BI} = L_{IU} = 2$;[7] $\phi_{B(U),\ell_{t(r)}} \in [-\frac{\pi}{3}, \frac{\pi}{3}]$, $\theta_{B(U),\ell_{t(r)}} \in [\frac{\pi}{6}, \frac{5\pi}{6}]$, $\tau_{BI(IU),\ell_{t(r)}} \in (0, 10^{-7}\text{sec}]$, $\alpha_{BI(IU),\ell_{t(r)}} \sim \mathcal{CN}(0,1)$. The detailed settings of the example conformal IRS topologies are tabulated in Table I. The LS, Direct, wideband direct (W-Direct) and wideband subspace (W-Subspace) schemes proposed in Section III. B, Section IV. A, Section IV. B. 1) and Section IV. B. 2), respectively, are simulated. Apart from the LS and W-Subspace schemes that can be combined with the All/Pair decoupling modes of (17), (18), respectively, the other schemes default to the Pair mode.

Table II compares the performance of different beamforming schemes with random IRS training patterns.[8] The performance of OMP is limited by its codebook resolution $(10^2 \times 10^2)$, which is less sensitive to the noise level. As the SoIs generally cover the angular parameters, the DFT beamforming achieves the best accuracy with a received SNR 7.7 dB and 6.3 dB higher than those of the random and On-Off counterparts, respectively. Hereinafter, we design the beamformers in a form of DFT matrices, determining their SoIs based on the coarse estimates from the On-Off scheme with one extra training frame.

---

[7]One can leverage the principal component analysis or minimum length description to estimate the number of paths [52]. To facilitate the evaluation of parameter recovery performance, L_{BI}, L_{IU} are assumed to be *a priori* known or perfectly estimated.

[8]The noise $\mathcal{N}_k \sim \mathcal{CN}(0, \sigma_n^2)$ is set with a fixed power level σ_n^2; $\epsilon(\phi)$, $\epsilon(\theta)$ denote the average rooted mean square error (RMSE) of $\{\phi_{B(U),\ell_{t(r)}}\}$ and $\{\theta_{B(U),\ell_{t(r)}}\}$, respectively; the signal-to-noise ratio (SNR) is defined as $\|\mathcal{Y}_k - \mathcal{N}_k\|_F^2/\|\mathcal{N}_k\|_F^2$. The random and On-Off schemes apply arbitrary and 0-1 coefficients, respectively, across $(P_{tr} + 1)$ frames; the DFT scheme uses 0-1 coefficients for a coarse estimation of one frame, followed by DFT coefficients with optimized SoIs for a fine estimation of P_{tr} frames. All the beamformers are normalized to have identical Frobenius norms.

TABLE I

TYPICAL SIMULATION SETTINGS OF CONFORMAL IRS TOPOLOGIES

Array Model	Radius	Structure Parameters	Channel Conditions
CyA	$r_{\mathrm{cy}} = 1.5\lambda_{\mathrm{c}}$	$\{\phi_{\mathrm{lb}}, \phi_{\mathrm{ub}}, d_{\mathrm{v}}\} = \left\{-\frac{\pi}{6}, \frac{\pi}{6}, \frac{\lambda_{\mathrm{c}}}{4}\right\}$	$\phi_{\mathrm{t(r)},\ell_{\mathrm{t(r)}}} \sim \mathcal{U}(-\frac{\pi}{3}, \frac{\pi}{3}), \theta_{\mathrm{t(r)},\ell_{\mathrm{t(r)}}} \sim \mathcal{U}(\frac{\pi}{6}, \frac{5\pi}{6})$
SA	$r_{\mathrm{s}} = 1.5\lambda_{\mathrm{c}}$	$\{\phi_{\mathrm{lb}}, \phi_{\mathrm{ub}}, \theta_{\mathrm{lb}}, \theta_{\mathrm{ub}}\} = \left\{-\pi, \pi, 0, \frac{\pi}{6}\right\}$	$\phi_{\mathrm{t(r)},\ell_{\mathrm{t(r)}}} \sim \mathcal{U}(-\pi, \pi), \theta_{\mathrm{t(r)},\ell_{\mathrm{t(r)}}} \sim \mathcal{U}(0, \frac{\pi}{3})$
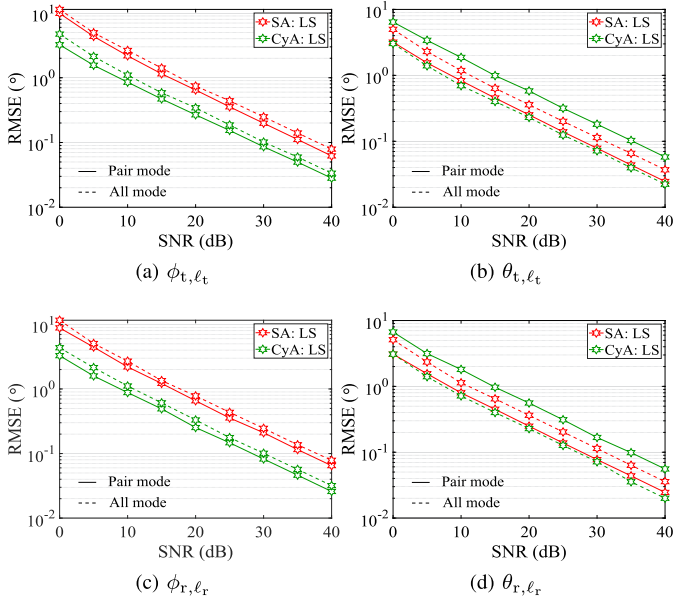
Fig. 3. RMSE of the decoupled channel parameters vs. SNR, $N_{\mathrm{h}} = N_{\mathrm{v}} = 6$, $P_{\mathrm{tr}} = 48$, $\epsilon = 1.0$.
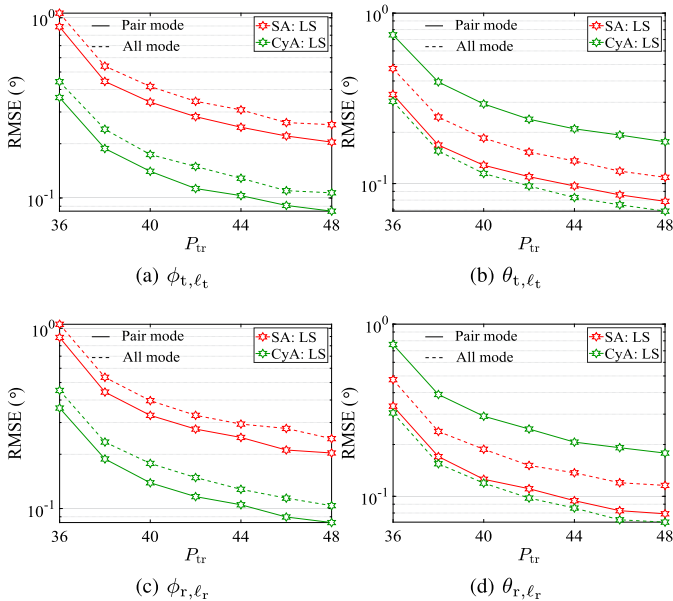
Fig. 4. RMSE of the decoupled channel parameters vs. the number of training frames, $N_{\mathrm{h}} = N_{\mathrm{v}} = 6$, SNR $= 30$ dB, $\epsilon = 1.0$.

Fig. 3 plots the RMSEs of the decoupled channel parameters on the IRS for the LS scheme versus the received SNR with $P_{\mathrm{tr}} = 48$. The performance of the LS scheme improves exponentially with respect to the increasing SNR. Moreover,

the LS-Pair version generally outperforms the LS-All version, benefiting from the additional power radiation information. The only exception is the elevation angle recovery for the CyA, which is due to the fact that the power radiation pattern of the CyA's vertical linear subarrays is a scalar coefficient that cannot be utilized effectively.

Fig. 4 plots the RMSEs for the LS scheme versus the number of training frames ($P_{\mathrm{tr}} \geq N_{\mathrm{I}}$) with SNR $= 30$ dB. By availing of more temporal measurements, the estimation accuracy can be effectively enhanced by an order of magnitude. Furthermore, the marginal benefit of increasing the training overhead gradually decreases as P_{tr} tends to larger values.

Fig. 5 plots the RMSEs for the OMP and Direct schemes in (22), (25) versus the received SNR with $P_{\mathrm{tr}} = 25$.[9] Due to the dominant complexity of iterative optimization, the Direct scheme can achieve high estimation accuracy comparable to the LS scheme with much fewer measurements. By contrast, the OMP scheme works well in the low-SNR region, but hits a performance bottleneck in the high-SNR region. This stems from the matching error of finite-resolution codebooks.

Fig. 6 plots the RMSEs for the OMP and Direct schemes versus the number of training frames with SNR $= 30$ dB. With dynamical computational complexity, the Direct scheme performs robustly against the varying amount of measurements; even a drastic decrease of P_{tr} will not result in a significant performance deterioration. The OMP scheme naturally cannot benefit much from the increased training overhead due to the limitation of codebook resolution.

Fig. 7 plots the RMSEs for the W-Direct and W-Subspace schemes versus the received SNR with $P_{\mathrm{tr}} = 16$, $K_{\mathrm{tr}} = 6$. By exploiting the information of frequency-dependent IRS training patterns, the wideband training schemes can compensate for the performance gap caused by the limited quantity of measurements. Concretely, the W-Direct scheme outperforms the W-Subspace scheme for the SA, while the latter works better for the CyA. This can be explained as follows: the CyA provides much less phase shift and power radiation information than the SA due to its repetitive row/column arrangement (see Fig. 2), whilst the optimization-based direct scheme entails higher requirements for the array structural features than the algebraic subspace scheme.

Fig. 8 plots the RMSEs for the W-Direct and W-Subspace schemes versus the number of training subcarriers with an SNR $= 30$ dB. As K_{tr} increases, the proposed schemes

---

[9]The hierarchical codebook of the OMP scheme consists of two levels; each level has an elevation/azimuth resolution of 20×40 and 30×30 for the SA and CyA, respectively. The corresponding window length are 2×4 and 3×3, respectively.

TABLE II

PERFORMANCE COMPARISON OF DIFFERENT BEAMFORMING SCHEMES

Beamforming		Random			On-Off						DFT		
Algorithm		OMP [14]			Standard ESPRIT			Unitary ESPRIT			Beamspace Unitary ESPRIT		
P_{tr}	σ_{n}^2	$\epsilon(\phi)$	$\epsilon(\theta)$	SNR	$\epsilon(\phi)$	$\epsilon(\theta)$	SNR	$\epsilon(\phi)$	$\epsilon(\theta)$	SNR	$\epsilon(\phi)$	$\epsilon(\theta)$	SNR
16	1.0	6.74e-1	5.43e-1	15.93	4.57e-2	3.56e-2	17.34	4.14e-2	3.16e-2	17.34	3.50e-2	2.08e-2	23.64
	0.1	6.48e-1	5.19e-1	25.80	1.51e-2	1.10e-2	27.25	1.33e-2	9.79e-3	27.25	1.11e-2	6.55e-3	33.58
32	1.0	6.88e-1	5.27e-1	15.95	3.33e-2	2.48e-2	17.32	2.92e-2	2.20e-2	17.32	2.24e-2	1.45e-2	23.67
	0.1	6.33e-1	5.10e-1	26.03	1.06e-2	7.84e-3	27.30	9.16e-3	6.97e-3	27.30	7.45e-3	4.55e-3	33.61
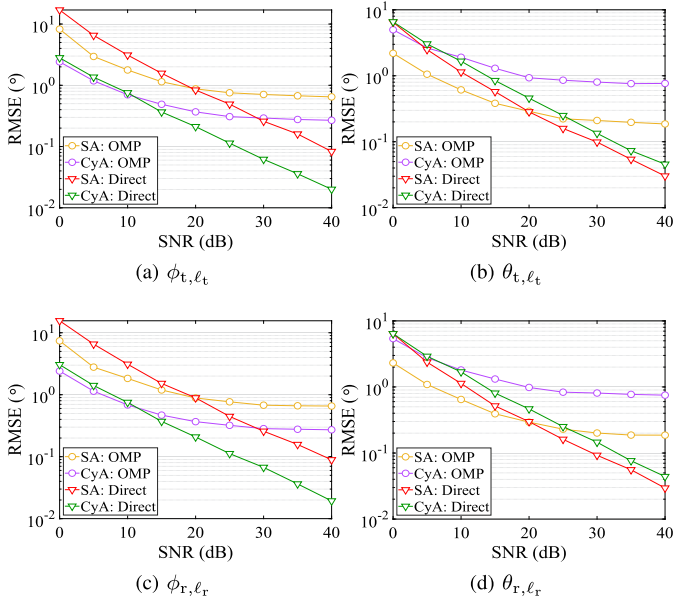
Fig. 5. RMSE of the decoupled channel parameters vs. SNR, $N_{\mathrm{h}} = N_{\mathrm{v}} = 6$, $P_{\mathrm{tr}} = 25$, $\epsilon = 1.0$.
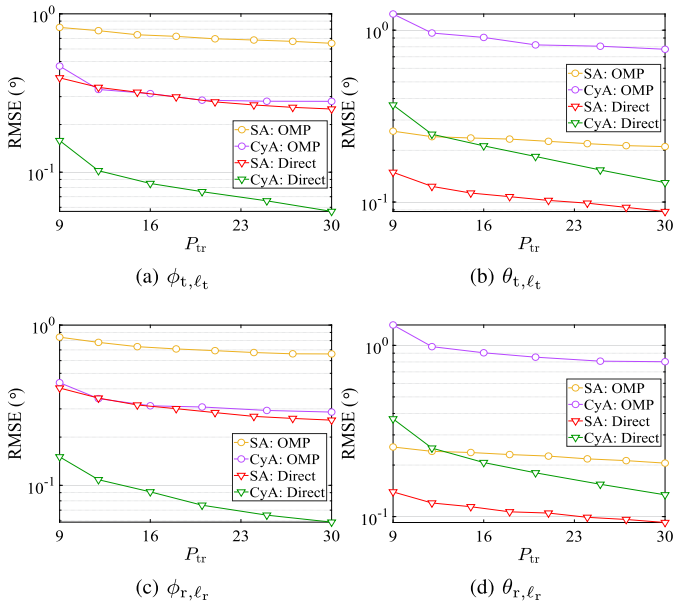
Fig. 7. RMSE of the decoupled channel parameters vs. SNR, $N_{\mathrm{h}} = N_{\mathrm{v}} = 6$, $P_{\mathrm{tr}} = 16$, $K_{\mathrm{tr}} = 6$, $\epsilon = 1.0$.

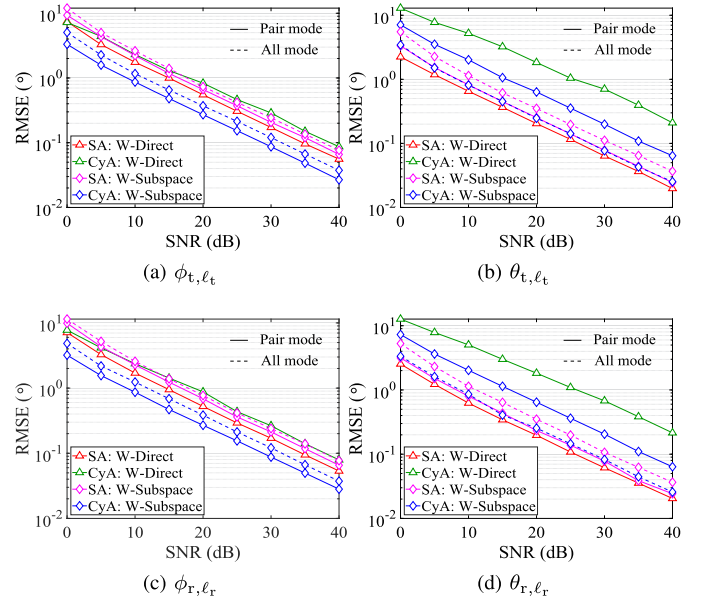Fig. 6. RMSE of the decoupled channel parameters vs. the number of training frames, $N_{\mathrm{h}} = N_{\mathrm{v}} = 6$, SNR = 30 dB, $\epsilon = 1.0$.
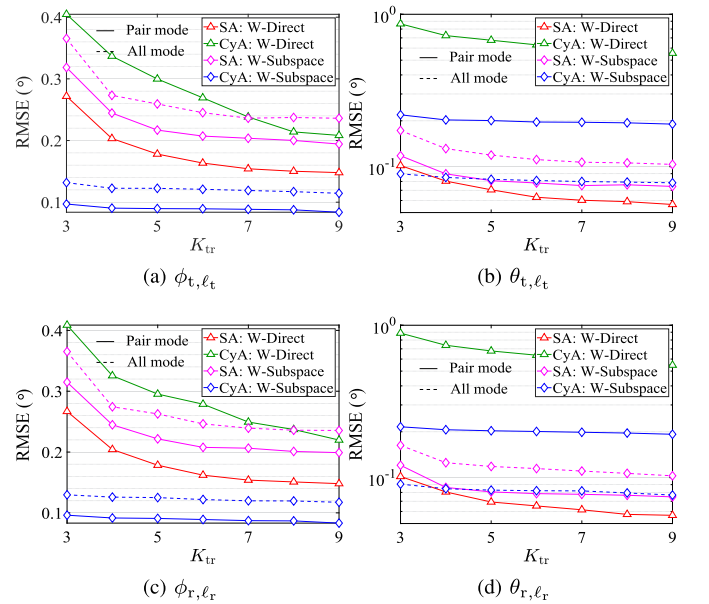
Fig. 8. RMSE of the decoupled channel parameters vs. the number of training subcarriers, $N_{\mathrm{h}} = N_{\mathrm{v}} = 6$, SNR = 30 dB, $P_{\mathrm{tr}} = 16$, $\epsilon = 1.0$.

achieve improved estimation performance with gradually diminishing marginal benefits, which is similar to the per-

formance trend versus P_{tr} as in Figs. 4, 6. This indicates that one can select only a small part of subcarriers to ensure
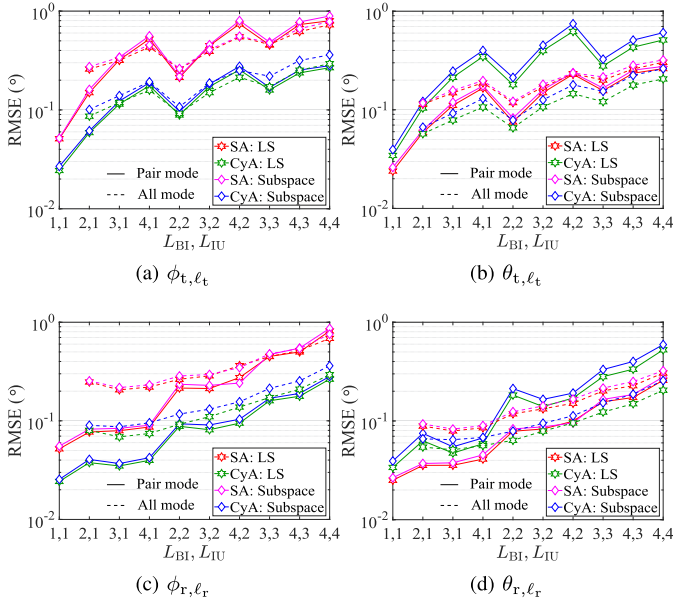
Fig. 9. RMSE of the decoupled channel parameters vs. the number of paths, $N_{\mathrm{h}} = N_{\mathrm{v}} = 6$, SNR $= 30$ dB, $\epsilon = 1.0$; LS: $P_{\mathrm{tr}} = 48$, $K_{\mathrm{tr}} = 1$; W-Subspace: $P_{\mathrm{tr}} = 16$, $K_{\mathrm{tr}} = 6$.

Fig. 11. RMSE of the environment mapping and user localization vs. SNR, $N_{\mathrm{h}} = N_{\mathrm{v}} = 6$, $K_{\mathrm{tr}} = 6$, $\epsilon = 1.0$; W-Subspace: $P_{\mathrm{tr}} = 16$, LS: $P_{\mathrm{tr}} = 48$.

Fig. 10. RMSE of the decoupled channel parameters vs. the power radiation coefficient, $N_{\mathrm{h}} = N_{\mathrm{v}} = 6$, SNR $= 30$ dB; LS: $P_{\mathrm{tr}} = 48$, $K_{\mathrm{tr}} = 1$; W-Subspace: $P_{\mathrm{tr}} = 16$, $K_{\mathrm{tr}} = 6$.
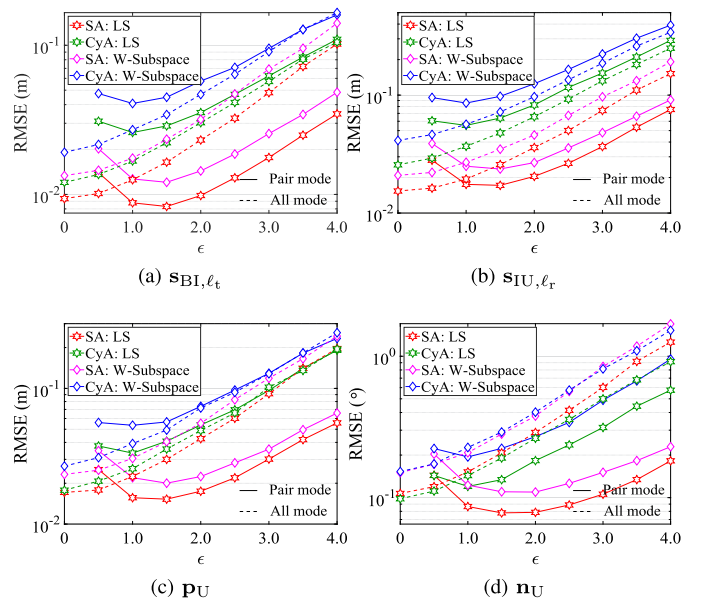
Fig. 12. RMSE of the environment mapping and user localization vs. the power radiation coefficient, $N_{\mathrm{h}} = N_{\mathrm{v}} = 6$, $K_{\mathrm{tr}} = 6$, SNR $= 30$ dB; W-Subspace: $P_{\mathrm{tr}} = 16$, LS: $P_{\mathrm{tr}} = 48$.

the training efficiency while controlling the computational overhead. Considering the performance-complexity efficiency of the proposed schemes, we leverage the LS and W-Subspace schemes hereinafter to evaluate the performance of channel estimation and environment mapping.

Fig. 9 plots the RMSEs versus the number of propagation paths, where the LS and W-Subspace schemes are performed with $P_{\mathrm{tr}} = 48, K_{\mathrm{tr}} = 1$ and $P_{\mathrm{tr}} = 16, K_{\mathrm{tr}} = 6$, respectively. As the total number of cascaded channel paths increases, the estimation error generally shows an upward trend. More specifically, when L_{BI} increases and L_{IU} remains unchanged, the parameter decoupling accuracy of $\mathbf{H}_{\mathrm{BI},k}$ gradually wors-
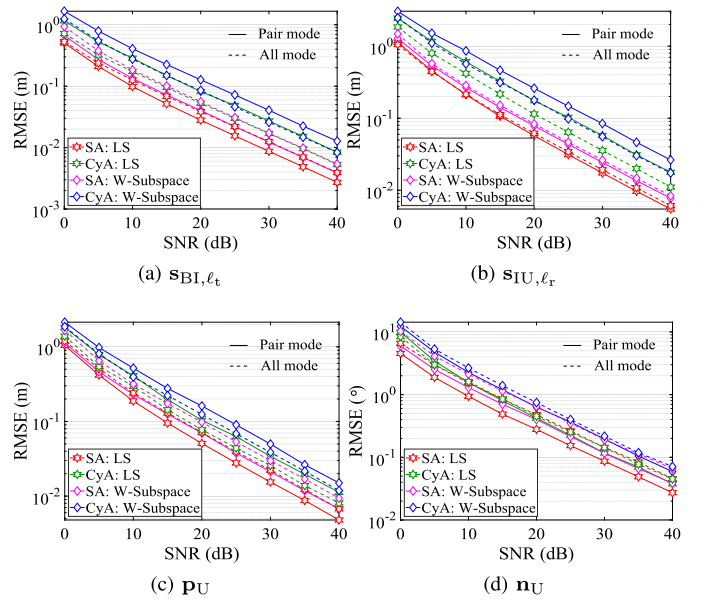
ens, whilst that of $\mathbf{H}_{\mathrm{IU},k}$ may experience a slight improvement (in conditions of small $L_{\mathrm{BI}}, L_{\mathrm{IU}}$) followed by a continuous deterioration, and vice versa. This can be explained as follows: too many mixed signal components naturally introduce negative uncertainties and disturbances into the channel estimation; however, by moderately adding more cascaded phase/amplitude constraints of a particular path, the recovery precision of this path can be effectively improved.

Fig. 10 plots the RMSEs versus the IRS power radiation coefficient with SNR $= 30$ dB. As ϵ increases from 0 to 4.0, the performance of the All mode continues to deteriorate, whilst that of the Pair mode first improves and then wors-

TABLE III
COMPUTATIONAL COMPLEXITY OF CHANNEL ESTIMATION APPROACHES

Algorithm	Complexity	Algorithm	Complexity
OMP [14]	$\mathcal{O}(M_{\mathrm{tr}}Q_{\mathrm{tr}}P_{\mathrm{tr}}N_{\mathrm{I}}L)$	BALS [16]	$\mathcal{O}(M_{\mathrm{tr}}Q_{\mathrm{tr}}P_{\mathrm{tr}}N_{\mathrm{I}})$ per iteration
LS	$\mathcal{O}(M_{\mathrm{tr}}Q_{\mathrm{tr}}P_{\mathrm{tr}}N_{\mathrm{I}})$	Direct	$\mathcal{O}(P_{\mathrm{tr}}N_{\mathrm{I}}^2 L)$ per iteration
W-Direct	$\mathcal{O}(K_{\mathrm{tr}}P_{\mathrm{tr}}N_{\mathrm{I}}^2 L)$ per iteration	W-Subspace	$\mathcal{O}(K_{\mathrm{tr}}P_{\mathrm{tr}}N_{\mathrm{I}}^2 L)$

ens. The former does not rely on the cascaded amplitude information from the radiation pattern of conformal IRSs, while the latter depends on effective amplitude constraints with an appropriate value of ϵ. In conclusion, a too small power radiation coefficient cannot lead to significant amplitude variations along the array aperture, whilst a too large one may cause a disappearance of weak signal responses at some unit cells.

Fig. 11 plots the RMSEs of the environment mapping applications versus the received SNR, where the LS and W-Subspace schemes are applied to a wideband system with $K_{\mathrm{tr}} = 6$ training subcarriers.[10] With the exactly decoupled channel parameters, the proposed schemes can support accurate localization and orientation with resolutions of lower than 1 cm and $0.1°$, respectively. By exploiting the additional information of IRS training coefficients, the W-Subspace scheme can achieve remarkable performance close to that of the LS scheme with only one-third of training measurements.

Fig. 12 plots the RMSEs of the environment mapping versus the coefficient of IRS power radiation with SNR = 30 dB. Since the channel estimation results can be averaged among multiple subcarriers, the LS scheme achieves superior performance. Naturally, the localization and orientation precision with respect to an increasing ϵ shows a variation tendency similar to the parameter recovery curves under All/Pair decoupling modes as in Fig. 10. This indicates that the specific circuit implementation of IRS unit cells significantly affects the reliability of channel estimation, as well as, the environment mapping.

Finally, Table III tabulates the computational complexity of the proposed channel estimation schemes. Provided with sufficient training frames or subcarriers, the LS and W-Subspace schemes perform robustly with fixed computational overhead. To compensate for the performance deterioration from limited training resources, the (W-)Direct scheme works with a dynamically adjustable complexity with respect to the flexible termination threshold. The complexity and performance of the BALS scheme heavily depend on its iteration threshold. Under most simulation conditions of limited training overhead, the BALS algorithm cannot work satisfactorily to return effective estimates of the channel parameters.

VII. CONCLUSION

We considered the channel estimation problem and environment mapping applications of IRS-empowered mmWave

MIMO-OFDM systems. In order to obtain accurate environmental information, we proposed a novel 3-D conformal IRS architecture composed of reflective unit cells arranged on a curved surface. We modeled the training signals as a third-order CP tensor, transforming the channel estimation problem into a tensor factorization task. By fully exploiting the spatial and frequency characteristics of conformal IRSs, we develop multiple channel estimation schemes that can apply to different condition of allocated training resources with the algebraic subspace and iterative optimization techniques. Based on the 3-D array topology of conformal IRSs, we achieved en exact decoupling of multipath parameters without estimation ambiguities. Finally, we implemented the environment mapping applications, determining the coordinates and orientations of scatterers and users. Numerical results showed that the proposed channel estimation schemes can precisely retrieve the channel parameters at the conformal IRS side, leading to a remarkable resolution of environment mapping.

APPENDIX
DERIVATIVES OF (20)

The first-order partial derivative of $\mathbf{e}_{\mathrm{g},\ell}$ in (20) with respect to $\phi_{\mathrm{t},\ell_{\mathrm{t}}}$ is written as

$$\frac{\partial \mathbf{e}_{\mathrm{g},\ell}}{\partial \phi_{\mathrm{t},\ell_{\mathrm{t}}}} = \frac{\partial \mathbf{e}_{\mathrm{g},\ell}}{\partial \mathbf{g}_{\mathrm{I,cas},\ell}} \frac{\partial \mathbf{g}_{\mathrm{I,cas},\ell}}{\partial \phi_{\mathrm{t},\ell_{\mathrm{t}}}}$$
$$= \left(\frac{1}{\|\mathbf{g}_{\mathrm{I,cas},\ell}\|_2} \mathbf{I}_{N_{\mathrm{I}}} - \frac{\mathbf{g}_{\mathrm{I,cas},\ell}\mathbf{g}_{\mathrm{I,cas},\ell}^T}{\|\mathbf{g}_{\mathrm{I,cas},\ell}\|_2^3} \right) \frac{\partial \mathbf{g}_{\mathrm{I,cas},\ell}}{\partial \phi_{\mathrm{t},\ell_{\mathrm{t}}}}, \tag{40}$$

where the nth entry of the derivative of $\mathbf{g}_{\mathrm{I,cas},\ell}$ with respect to $\phi_{\mathrm{t},\ell_{\mathrm{t}}}$ is written as

$$\frac{\partial [\mathbf{g}_{\mathrm{I,cas},\ell}]_n}{\partial \phi_{\mathrm{t},\ell_{\mathrm{t}}}} = \frac{\epsilon}{2} \boldsymbol{\nu}_n^T \frac{\partial \mathbf{d}(\phi_{\mathrm{t},\ell_{\mathrm{t}}}, \theta_{\mathrm{t},\ell_{\mathrm{t}}})}{\partial \phi_{\mathrm{t},\ell_{\mathrm{t}}}} \varepsilon \left(\boldsymbol{\nu}_n^T \mathbf{d}(\phi_{\mathrm{t},\ell_{\mathrm{t}}}, \theta_{\mathrm{t},\ell_{\mathrm{t}}}) \right)$$
$$\times f_+^{\frac{\epsilon}{2}-1} \left(\boldsymbol{\nu}_n^T \mathbf{d}(\phi_{\mathrm{t},\ell_{\mathrm{t}}}, \theta_{\mathrm{t},\ell_{\mathrm{t}}}) \right)$$
$$\times f_+^{\frac{\epsilon}{2}} \left(\boldsymbol{\nu}_n^T \mathbf{d}(\phi_{\mathrm{r},\ell_{\mathrm{r}}}, \theta_{\mathrm{r},\ell_{\mathrm{r}}}) \right), \tag{41}$$

with $\varepsilon(\cdot)$ being the Heaviside step function. Similarly, the partial derivative of $\mathbf{e}_{\mathrm{g},\ell}$ with respect to $\theta_{\mathrm{t},\ell_{\mathrm{t}}}$ can be calculated by following (40), (41), except for the term of $\frac{\partial \mathbf{d}(\phi_{\mathrm{t},\ell_{\mathrm{t}}}, \theta_{\mathrm{t},\ell_{\mathrm{t}}})}{\partial \theta_{\mathrm{t},\ell_{\mathrm{t}}}}$. The first order derivatives of $\mathbf{d}(\phi_{\mathrm{t},\ell_{\mathrm{t}}}, \theta_{\mathrm{t},\ell_{\mathrm{t}}})$ with respect to $\phi_{\mathrm{t},\ell_{\mathrm{t}}}$, $\theta_{\mathrm{t},\ell_{\mathrm{t}}}$ are respectively expressed as follows:

$$\frac{\partial \mathbf{d}(\phi_{\mathrm{t},\ell_{\mathrm{t}}}, \theta_{\mathrm{t},\ell_{\mathrm{t}}})}{\partial \phi_{\mathrm{t},\ell_{\mathrm{t}}}} = [-\sin\phi_{\mathrm{t},\ell_{\mathrm{t}}}\sin\theta_{\mathrm{t},\ell_{\mathrm{t}}}, \cos\phi_{\mathrm{t},\ell_{\mathrm{t}}}\sin\theta_{\mathrm{t},\ell_{\mathrm{t}}}, 0]^T, \tag{42a}$$

$$\frac{\partial \mathbf{d}(\phi_{\mathrm{t},\ell_{\mathrm{t}}}, \theta_{\mathrm{t},\ell_{\mathrm{t}}})}{\partial \theta_{\mathrm{t},\ell_{\mathrm{t}}}} = [\cos\phi_{\mathrm{t},\ell_{\mathrm{t}}}\cos\theta_{\mathrm{t},\ell_{\mathrm{t}}}, \sin\phi_{\mathrm{t},\ell_{\mathrm{t}}}\cos\theta_{\mathrm{t},\ell_{\mathrm{t}}},$$
$$- \sin\theta_{\mathrm{t},\ell_{\mathrm{t}}}]^T. \tag{42b}$$

---

[10]The device coordinates and orientations are randomized such that the channel parameters fall into the predefined distribution ranges. The LoS and NLoS paths are randomized with maximum length bounds of 10 m and 20 m, respectively.

References

[1] M. Xiao *et al.*, "Millimeter wave communications for future mobile networks," *IEEE J. Sel. Areas Commun.*, vol. 35, no. 9, pp. 1909–1935, Sep. 2017.

[2] M. Matthaiou, O. Yurduseven, H. Q. Ngo, D. Morales-Jimenez, S. L. Cotton, and V. F. Fusco, "The road to 6G: Ten physical layer challenges for communications engineers," *IEEE Commun. Mag.*, vol. 59, no. 1, pp. 64–69, Jan. 2021.

[3] J. Zhang *et al.*, "Prospective multiple antenna technologies for beyond 5G," *IEEE J. Sel. Areas Commun.*, vol. 38, no. 8, pp. 1637–1660, Aug. 2020.

[4] S. Hu, F. Rusek, and O. Edfors, "Beyond massive MIMO: The potential of data transmission with large intelligent surfaces," *IEEE Trans. Signal Process.*, vol. 66, no. 10, pp. 2746–2758, May 2018.

[5] Y. Han, W. Tang, S. Jin, C. Wen, and X. Ma, "Large intelligent surface-assisted wireless communication exploiting statistical CSI," *IEEE Trans. Veh. Technol.*, vol. 68, no. 8, pp. 8238–8242, Jun. 2019.

[6] W. Tang *et al.*, "MIMO transmission through reconfigurable intelligent surface: System design, analysis, and implementation," *IEEE J. Sel. Areas Commun.*, vol. 38, no. 11, pp. 2683–2699, Nov. 2020.

[7] W. Tang *et al.*, "Wireless communications with reconfigurable intelligent surface: Path loss modeling and experimental measurement," *IEEE Trans. Wireless Commun.*, vol. 20, no. 1, pp. 421–439, Jan. 2021.

[8] Q. Wu and R. Zhang, "Towards smart and reconfigurable environment: Intelligent reflecting surface aided wireless network," *IEEE Commun. Mag.*, vol. 58, no. 1, pp. 106–112, Nov. 2020.

[9] X. Yuan *et al.*, "Reconfigurable-intelligent-surface empowered wireless communications: Challenges and opportunities," *IEEE Wireless Commun.*, vol. 28, no. 2, pp. 136–143, Apr. 2021.

[10] X. Yang, C.-K. Wen, and S. Jin, "MIMO detection for reconfigurable intelligent surface-assisted millimeter wave systems," *IEEE J. Sel. Areas Commun.*, vol. 38, no. 8, pp. 1777–1792, Aug. 2020.

[11] T. Hou, Y. Liu, Z. Song, X. Sun, and Y. Chen, "MIMO-NOMA networks relying on reconfigurable intelligent surface: A signal cancellation-based design," *IEEE Trans. Commun.*, vol. 68, no. 11, pp. 6932–6944, Nov. 2020.

[12] B. Feng, Y. Wu, M. Zheng, X.-G. Xia, Y. Wang, and C. Xiao, "Large intelligent surface aided physical layer security transmission," *IEEE Trans. Signal Process.*, vol. 68, pp. 5276–5291, 2020.

[13] H. Wymeersch, J. He, B. Denis, A. Clemente, and M. Juntti, "Radio localization and mapping with reconfigurable intelligent surfaces: Challenges, opportunities, and research directions," *IEEE Veh. Technol. Mag.*, vol. 15, no. 4, pp. 52–61, Dec. 2020.

[14] S. Ma, W. Shen, J. An, and L. Hanzo, "Wideband channel estimation for IRS-aided systems in the face of beam squint," *IEEE Trans. Wireless Commun.*, vol. 20, no. 10, pp. 6240–6253, Oct. 2021.

[15] J. He, H. Wymeersch, and M. Juntti, "Channel estimation for RIS-aided mmWave MIMO systems via atomic norm minimization," *IEEE Trans. Wireless Commun.*, vol. 20, no. 9, pp. 5786–5797, Sep. 2021.

[16] L. Wei, C. Huang, G. C. Alexandropoulos, C. Yuen, Z. Zhang, and M. Debbah, "Channel estimation for RIS-empowered multi-user MISO wireless communications," *IEEE Trans. Commun.*, vol. 69, no. 6, pp. 4144–4157, Mar. 2021.

[17] D. Mishra and H. Johansson, "Channel estimation and low-complexity beamforming design for passive intelligent surface assisted MISO wireless energy transfer," in *Proc. IEEE Int. Conf. Acoust., Speech Signal Process. (ICASSP)*, May 2019, pp. 4663–4689.

[18] Z. Wang, L. Liu, and S. Cui, "Channel estimation for intelligent reflecting surface assisted multiuser communications: Framework, algorithms, and analysis," *IEEE Trans. Wireless Commun.*, vol. 19, no. 10, pp. 6607–6620, Oct. 2020.

[19] Z.-Q. He and X. Yuan, "Cascaded channel estimation for large intelligent metasurface assisted massive MIMO," *IEEE Wireless Commun. Lett.*, vol. 9, no. 2, pp. 210–214, Feb. 2020.

[20] H. Liu, X. Yuan, and Y.-J.-A. Zhang, "Matrix-calibration-based cascaded channel estimation for reconfigurable intelligent surface assisted multiuser MIMO," *IEEE J. Sel. Areas Commun.*, vol. 38, no. 11, pp. 2621–2636, Nov. 2020.

[21] Y. Lin, S. Jin, M. Matthaiou, and X. You, "Tensor-based algebraic channel estimation for hybrid IRS-assisted MIMO-OFDM," *IEEE Trans. Wireless Commun.*, vol. 20, no. 6, pp. 3770–3784, Jun. 2021.

[22] A. Taha, M. Alrabeiah, and A. Alkhateeb, "Enabling large intelligent surfaces with compressive sensing and deep learning," *IEEE Access*, vol. 9, pp. 44304–44321, 2021.

[23] C. Hu, L. Dai, S. Han, and X. Wang, "Two-timescale channel estimation for reconfigurable intelligent surface aided wireless communications," *IEEE Trans. Commun.*, vol. 69, no. 11, pp. 7736–7747, Nov. 2021.

[24] X. Guan, Q. Wu, and R. Zhang, "Anchor-assisted channel estimation for intelligent reflecting surface aided multiuser communication," *IEEE Trans. Wireless Commun.*, early access, Nov. 13, 2021, doi: 10.1109/TWC.2021.3123674.

[25] Y. Lin, S. Jin, M. Matthaiou, and X. You, "Channel estimation and user localization for IRS-assisted MIMO-OFDM systems," *IEEE Trans. Wireless Commun.*, vol. 21, no. 4, pp. 2320–2335, Apr. 2022.

[26] S. E. Zegrar, L. Afeef, and H. Arslan, "A general framework for RIS-aided mmWave communication networks: Channel estimation and mobile user tracking," 2020, *arXiv:2009.01180*.

[27] W. Wang and W. Zhang, "Joint beam training and positioning for intelligent reflecting surfaces assisted millimeter wave communications," *IEEE Trans. Wireless Commun.*, vol. 20, no. 10, pp. 6282–6297, Oct. 2021.

[28] I. Domanov and L. De Lathauwer, "On the uniqueness of the canonical polyadic decomposition of third-order tensors—Part I: Basic results and uniqueness of one factor matrix," *SIAM J. Matrix Anal. Appl.*, vol. 34, no. 3, pp. 855–875, Jan. 2013.

[29] I. Domanov and L. D. Lathauwer, "On the uniqueness of the canonical polyadic decomposition of third-order tensors—Part II: Uniqueness of the overall decomposition," *SIAM J. Matrix Anal. Appl.*, vol. 34, no. 3, pp. 876–903, 2013.

[30] H. Li, W. Cai, Y. Liu, M. Li, Q. Liu, and Q. Wu, "Intelligent reflecting surface enhanced wideband MIMO-OFDM communications: From practical model to reflection optimization," *IEEE Trans. Commun.*, vol. 69, no. 7, pp. 4807–4820, Jul. 2021.

[31] N. Vervliet, O. Debals, L. Sorber, M. Van Barel, and L. D. Lathauwer. (Mar. 2016). *Tensorlab 3.0*. [Online]. Available: https://www.tensorlab.net/

[32] Z. Lin, T. Lv, and P. T. Mathiopoulos, "3-D indoor positioning for millimeter-wave massive MIMO systems," *IEEE Trans. Commun.*, vol. 66, no. 6, pp. 2472–2486, Jun. 2018.

[33] M.-T. Martínez-Inglés, D. P. Gaillot, J. Pascual-García, J.-M. Molina-García-Pardo, M. Lienard, and J.-V. Rodríguez, "Deterministic and experimental indoor mmW channel modeling," *IEEE Antennas Wireless Propag. Lett.*, vol. 13, pp. 1047–1050, 2014.

[34] J. Yang *et al.*, "A geometry-based stochastic channel model for the millimeter-wave band in a 3GPP high-speed train scenario," *IEEE Trans. Veh. Technol.*, vol. 67, no. 5, pp. 3853–3865, May 2018.

[35] Y. Huang and K. Boyle, *Antennas: From Theory to Practice*. Chichester, U.K.: Wiley, 2008.

[36] W. L. Stutzman and G. A. Thiele, *Antenna Theory Design*, 3rd ed. New York, NY, USA: Wiley, 2012.

[37] P. Yang, F. Yang, and Z.-P. Nie, "DOA estimation with sub-array divided technique and interporlated ESPRIT algorithm on a cylindrical conformal array antenna," *Prog. Electromagn. Res.*, vol. 103, pp. 201–216, 2010.

[38] X.-F. Gao, P. Li, X.-H. Hao, G.-L. Li, and Z.-J. Kong, "A novel DOA estimation algorithm using directional antennas in cylindrical conformal arrays," *Defence Technol.*, vol. 17, no. 3, pp. 1042–1051, Jun. 2021.

[39] R. Sun, W. Wang, L. Chen, G. Wei, and W. Zhang, "Diagnosis of intelligent reflecting surface in millimeter-wave communication systems," *IEEE Trans. Wireless Commun.*, early access, Nov. 15, 2021, doi: 10.1109/TWC.2021.3125734.

[40] S. Zhang, H. Zhang, B. Di, Y. Tan, Z. Han, and L. Song, "Beyond intelligent reflecting surfaces: Reflective-transmissive metasurface aided communications for full-dimensional coverage extension," *IEEE Trans. Veh. Technol.*, vol. 69, no. 11, pp. 13905–13909, Nov. 2020.

[41] M. D. Zoltowski, M. Haardt, and C. P. Mathews, "Closed-form 2-D angle estimation with rectangular arrays in element space or beamspace via unitary ESPRIT," *IEEE Trans. Signal Process.*, vol. 44, no. 2, pp. 316–328, Feb. 1996.

[42] A. Bunse-Gerstner, R. Byers, and V. Mehrmann, "Numerical methods for simultaneous diagonalization," *SIAM J. Matrix Anal. Appl.*, vol. 14, no. 4, pp. 927–949, Oct. 1993.

[43] J. Zhang, D. Rakhimov, and M. Haardt, "Gridless channel estimation for hybrid mmWave MIMO systems via tensor-ESPRIT algorithms in DFT beamspace," *IEEE J. Sel. Topics Signal Process.*, vol. 15, no. 3, pp. 816–831, Apr. 2021.

[44] V. V. Reddy, A. W. H. Khong, and B. P. Ng, "Unambiguous speech DOA estimation under spatial aliasing conditions," *IEEE/ACM Trans. Audio, Speech, Language Process.*, vol. 22, no. 12, pp. 2133–2145, Dec. 2014.

[45] A. Bohlender, A. Spriet, W. Tirry, and N. Madhu, "Least-squares DOA estimation with an informed phase unwrapping and full bandwidth robustness," in *Proc. IEEE Int. Conf. Acoust., Speech Signal Process. (ICASSP)*, May 2020, pp. 4841–4845.

[46] H. P. Gavin, "The Levenberg–Marquardt algorithm for nonlinear least squares curve-fitting problems," Dept. Civil Environ. Eng., Duke Univ., Durham, NC, USA, 2019.

[47] S. Qin, Y. D. Zhang, and M. G. Amin, "Generalized coprime array configurations for direction-of-arrival estimation," *IEEE Trans. Signal Process.*, vol. 63, no. 6, pp. 1377–1390, Mar. 2015.

[48] J. Kennedy and R. Eberhart, "Particle swarm optimization," in *Proc. ICNN*, Nov. 1995, pp. 1942–1948.

[49] J. E. Gentle, *Matrix Algebra: Theory, Computations, and Applications in Statistics*, 2nd ed. Cham, Switzerland: Springer, 2017.

[50] G. H. Golub and C. F. Van Loan, *Matrix Computation*, 4th ed. Baltimore, MD, USA: Johns Hopkins Univ. Press, 2013.

[51] J. S. Dai, "Euler–Rodrigues formula variations, quaternion conjugation and intrinsic connections," *Mechanism Mach. Theory*, vol. 92, pp. 144–152, Oct. 2015.

[52] K. Liu, J. P. C. L. da Costa, H. C. So, L. Huang, and J. Ye, "Detection of number of components in CANDECOMP/PARAFAC models via minimum description length," *Digit. Signal Process.*, vol. 51, pp. 110–123, Apr. 2016.

Yuxing Lin (Student Member, IEEE) received the B.S. degree in information engineering from Southeast University, Nanjing, China, in 2016, where he is currently pursuing the Ph.D. degree with the School of Information Science and Engineering. His research interests include massive MIMO, millimeter wave wireless communications, hybrid beamforming, channel estimation, beam training/tracking, tensor signal processing, and intelligent reconfigurable surface-assisted communications.

Shi Jin (Senior Member, IEEE) received the B.S. degree in communications engineering from the Guilin University of Electronic Technology, Guilin, China, in 1996, the M.S. degree from the Nanjing University of Posts and Telecommunications, Nanjing, China, in 2003, and the Ph.D. degree in information and communications engineering from Southeast University, Nanjing, in 2007. From June 2007 to October 2009, he was a Research Fellow with the Adastral Park Research Campus, University College London, London, U.K. He is currently with the Faculty of the National Mobile Communications Research Laboratory, Southeast University. His research interests include space time wireless communications, random matrix theory, and information theory. He and his coauthors have been awarded the 2011 IEEE Communications Society Stephen O. Rice Prize Paper Award in the field of communication theory and the 2010 Young Author Best Paper Award by the IEEE Signal Processing Society. He serves as an Associate Editor for the IEEE TRANSACTIONS ON WIRELESS COMMUNICATIONS, IEEE COMMUNICATIONS LETTERS, and *IET Communications*.

Michail Matthaiou (Senior Member, IEEE) was born in Thessaloniki, Greece, in 1981. He received the Diploma degree (5 years) in electrical and computer engineering from the Aristotle University of Thessaloniki, Greece, in 2004, the M.Sc. degree (Hons.) in communication systems and signal processing from the University of Bristol, U.K., in 2005, and the Ph.D. degree from The University of Edinburgh, U.K., in 2008.

From September 2008 to May 2010, he was with the Institute for Circuit Theory and Signal Processing, Munich University of Technology (TUM), Germany, working as a Post-Doctoral Research Associate. He is currently a Professor of communications engineering and signal processing and the Deputy Director of the Centre for Wireless Innovation (CWI), Queen's University Belfast, U.K., after holding an Assistant Professor position at the Chalmers University of Technology, Sweden. His research interests span signal processing for wireless communications, beyond massive MIMO, intelligent reflecting surfaces, mm-wave/THz systems, and deep learning for communications. He and his coauthors received the IEEE Communications Society (ComSoc) Leonard G. Abraham Prize in 2017. He also holds the ERC Consolidator Grant BEATRICE (2021–2026) focused on the interface between information and electromagnetic theories. He was awarded the prestigious 2018/2019 Royal Academy of Engineering/The Leverhulme Trust Senior Research Fellowship and also received the 2019 EURASIP Early Career Award. His team was also the Grand Winner of the 2019 Mobile World Congress Challenge. He was a recipient of the 2011 IEEE ComSoc Best Young Researcher Award for the Europe, Middle East and Africa Region, and a co-recipient of the 2006 IEEE Communications Chapter Project Prize for the best M.Sc. dissertation in the area of communications. He has coauthored papers that received Best Paper Awards at the 2018 IEEE WCSP and 2014 IEEE ICC. In 2014, he received the Research Fund for International Young Scientists from the National Natural Science Foundation of China. He is also the Editor-in-Chief of *Physical Communication* (Elsevier), a Senior Editor of the IEEE WIRELESS COMMUNICATIONS LETTERS, and an Associate Editor of the IEEE JOURNAL ON SELECTED AREAS IN COMMUNICATIONS Series on Machine Learning for Communications and Networks.

Xiaohu You (Fellow, IEEE) received the B.S., M.S., and Ph.D. degrees in electrical engineering from the Nanjing Institute of Technology, Nanjing, China, in 1982, 1985, and 1989, respectively. From 1987 to 1989, he was a Lecturer with the Nanjing Institute of Technology. Since 1990, he has been with Southeast University, first as an Associate Professor and then as a Professor. He contributed over 40 IEEE journal articles and two books in the areas of adaptive signal processing and neural networks and their applications to communication systems. He was the Premier Foundation Investigator of the China National Science Foundation. From 1999 to 2002, he was the Principal Expert of the C3G Project, responsible for organizing China's 3G mobile communications research and development activities. From 2001 to 2006, he was the Principal Expert of the National 863 FuTURE Project. His research interests include mobile communications, adaptive signal processing, and artificial neural networks with applications to communications and biomedical engineering. In 2012, he was selected as an IEEE Fellow for his contributions to the development of mobile communications in China. He received the Excellent Paper Award from the China Institute of Communications in 1987 and the Elite Outstanding Young Teacher Award from Southeast University in 1990, 1991, and 1993. He is also the Chairperson of the IEEE Nanjing Section.